

Changes in apparent temperature and PM_{2.5} around the Beijing-Tianjin megalopolis under greenhouse gas and stratospheric aerosol intervention scenarios

Jun Wang¹, John C. Moore^{1,2*}, Liyun Zhao^{1*}

¹State Key Laboratory of Earth Surface Processes and Resource Ecology, Faculty of Geographical Science, Beijing Normal University, Beijing 100875, China

²Arctic Center, University of Lapland, Rovaniemi, Finland

Correspondence to: zhaoliyun@bnu.edu.cn, john.moore.bnu@gmail.com

Abstract. Apparent temperatures (AP) and ground level aerosol pollution (PM_{2.5}) are important factors in human health, particularly in rapidly growing urban centres in the developing world. We quantify how changes in apparent temperature – that is a combination of 2 m air temperature, relative humidity and surface wind speed, and PM_{2.5} concentrations – that depend on the same meteorological factors along with future industrial emission policy, may impact people in the greater Beijing region. Four Earth System Models (ESM) simulations of the modest greenhouse emissions RCP4.5, the “business-as-usual” RCP8.5 and the stratospheric aerosol intervention G4 geoengineering scenarios are downscaled using both a 10 km resolution dynamic model (WRF), and a statistically approach (ISIMIP). We use multiple linear regression models to simulate changes in PM_{2.5} and the contributions meteorological factors make in controlling seasonal AP and PM_{2.5}. WRF produces warmer winters and cooler summers than does ISIMIP both now and in the future. These differences mean that estimates of numbers of days with extreme apparent temperatures vary systematically with downscaling method, as well as between climate models and scenarios. Air temperature changes dominate differences in apparent temperatures between future scenarios even more than they do at present because the reductions in humidity expected under solar geoengineering are overwhelmed by rising vapor pressure due to rising temperatures and the lower windspeeds expected in the region in all future scenarios. Compared with the 2010s, PM_{2.5} concentration is projected to decrease 5.4 µg/m³ in the Beijing-Tianjin province under the G4 scenario during the 2060s from the WRF downscaling, but decrease by 7.6 µg/m³ using ISIMIP. The relative risk of 5 diseases decreases by 1.1%-6.7% in G4/RCP4.5/RCP8.5 using ISIMIP, but have smaller decrease (0.7%-5.2%) using WRF. Temperature and humidity differences between scenarios change the relative risk of disease from PM_{2.5} such that G4 results in 1-3% higher health risks than RCP4.5. Urban centres see larger rises in extreme apparent temperatures than rural surroundings due to differences in land surface type, and since these are also the most densely populated, health impacts will be dominated by the larger rises in apparent temperatures in these urban areas.

41 **500 character non-technical text**

42 Apparent temperatures and PM_{2.5} pollution depends on humidity and wind speed in
43 addition to surface temperature and impacts human health and comfort. Apparent
44 temperatures will reach dangerous levels more commonly in future because of water
45 vapor pressure rises and lower expected wind speeds, but these will also drive change
46 in PM_{2.5}. Solar geoengineering can reduce the frequency of extreme events significantly
47 relative to modest, and especially “business as usual” greenhouse scenarios.
48
49

50 **1. Introduction**

51 Global mean surface temperature has increased by 0.92°C (0.68-1.17°C) during 1880-
52 2012 (IPCC, 2021), which naturally also impacts the human living environment
53 (Kraaijenbrink et al., 2017; Garcia et al., 2018). However, neither land surface
54 temperature nor near-surface air temperature can adequately represent the temperature
55 we experience. Apparent temperature (AP), that is how the temperature feels, is
56 formulated to reflect human thermal comfort and is probably a more important
57 indication of health than daily maximum or minimum temperatures (Fischer et al., 2013;
58 Matthews et al., 2017; Wang et al., 2021). There are various approaches to estimating
59 how the weather conditions affect comfort, but apparent temperature is governed by air
60 temperature, humidity and wind speed (Steadman 1984; Steadman 1994). These are
61 known empirically to affect human thermal comfort (Jacobs et al., 2013), and thresholds
62 have been designed to indicate danger and health risks under extreme heat events (Ho
63 et al., 2016). Analysis of historical apparent temperatures in China (Wu et al., 2017; Chi
64 et al., 2018; Wang et al., 2019), Australia (Jacobs et al., 2013), and the USA (Grundstein
65 et al., 2011) all find that apparent temperature is increasing faster than air temperature.
66 This is due to both decreasing wind speeds and, especially to increasing vapor pressure
67 (Song et al., 2022).
68

69 As the world warms, apparent temperature is expected to rise faster than air
70 temperatures in the future (Li et al., 2018; Song et al., 2022). Hence, humans, and other
71 species, will face more heat-related stress but less cold-related environmental stress in
72 the warmer future (Wang et al., 2018; Zhu et al., 2019). Since most of the population is
73 now urban, the conditions in cities will determine how tolerable are future climates for
74 much of humanity, while the differences in thermal comfort between urbanized and
75 rural regions will be a factor in driving urbanization. Reliable estimates of future urban
76 temperatures and their rural surroundings require methods to improve on standard
77 climate model resolution to adequately represent the different land surface types;
78 especially the rapid and accelerating changes in land cover in the huge urban areas
79 characteristic of sprawling developments in the developing world. This is usually done
80 with either statistical or dynamic downscaling approaches, and in this article we
81 examine both methods.

82

83 In early 2013, Beijing encountered a serious pollution incident. The concentration of
84 $PM_{2.5}$ (particles with diameters less than or equal to $2.5 \mu m$ in the atmosphere) exceeded
85 $500 \mu g/m^3$ (Wang et al., 2014). Following this event and its expected impacts on human
86 health (Guan et al., 2016; Fan et al., 2021) and the economy (Maji et al., 2018; Wang
87 et al., 2020), the Beijing municipal government launched the Clean Air Action Plan in
88 2013. The annual mean concentration of $PM_{2.5}$ in Beijing-Tianjin-Hebei region
89 decreased from $90.6 \mu g/m^3$ in 2013 to $56.3 \mu g/m^3$ in 2017, a decrease of about 38%
90 (Zhang et al., 2019), although this is still more than double the EU air quality standard
91 ($25 \mu g/m^3$) and above the Chinese FGNS (First Grand National Standard) of $35 \mu g/m^3$.
92 The concentration of $PM_{2.5}$ is related to anthropogenic emissions, but also dependent
93 on meteorological conditions (Chen et al., 2020). Simulations suggested that 80% of
94 the 2013-2017 lowering of $PM_{2.5}$ concentration came from emission reductions in
95 Beijing (Chen et al. 2019). Humidity and temperature are the main meteorological
96 factors affecting $PM_{2.5}$ concentration in Beijing in summer, while humidity and wind
97 speed are the main factors in winter (Chen et al., 2018). Simulations driven by different
98 RCP emission scenarios with fixed meteorology for the year 2010 suggest that $PM_{2.5}$
99 concentration will meet FGNS under RCP2.6, RCP4.5 and RCP8.5 in Beijing-Tianjin-
100 Hebei after 2040 (Li et al., 2016).

101

102 The focus here is in the differences in apparent temperature and $PM_{2.5}$ that may arise
103 from solar geoengineering (that is reduction in incoming short-wave radiation to offset
104 longwave absorption by greenhouse gases) via stratospheric aerosol intervention (SAI),
105 and pure greenhouse gas climates. We use all four climate models that have provided
106 sufficient data from the G4 scenario described by the Geoengineering Model
107 Intercomparison Project (GeoMIP). G4 specifies sulfates as the aerosol, and greenhouse
108 gas emissions from the RCP4.5 scenario (Kravitz et al., 2011). The impacts of G4 on
109 surface temperature and precipitation have been discussed at regional scales (Yu et al.,
110 2015) and both are lowered relative to RCP4.5. Some studies have focused on regional
111 impact of SAI on apparent or wet bulb temperatures: in Europe, (Jones et al., 2018);
112 East Asia (Kim et al., 2020); and the Maritime Continent (Kuswanto et al., 2021). But
113 none of these studies have considered apparent temperature at scales appropriate for
114 rapidly urbanizing regions such as on the North China Plain. The only study to date on
115 SAI impacts on $PM_{2.5}$ pollution was a coarse resolution ($4^\circ \times 5^\circ$) global scale model with
116 sophisticated chemistry (Eastham et al., 2018). They simulated aerosol rainout from the
117 stratosphere to ground level, leading to an eventual increase in ground level $PM_{2.5}$.
118 Eastham et al. (2018) concluded that SAI changes in tropospheric and stratospheric
119 ozone dominated $PM_{2.5}$ impacts on global mortality. However, this study included only
120 a first-order estimate of temperature and precipitation change on $PM_{2.5}$ concentration
121 under geoengineering, and also did not consider the situation in a highly polluted urban
122 environment such as included in our domain, and which is typical of much of the
123 developing world.

124

125 The greater Beijing megalopolis lies in complex terrain, surrounded by hills and

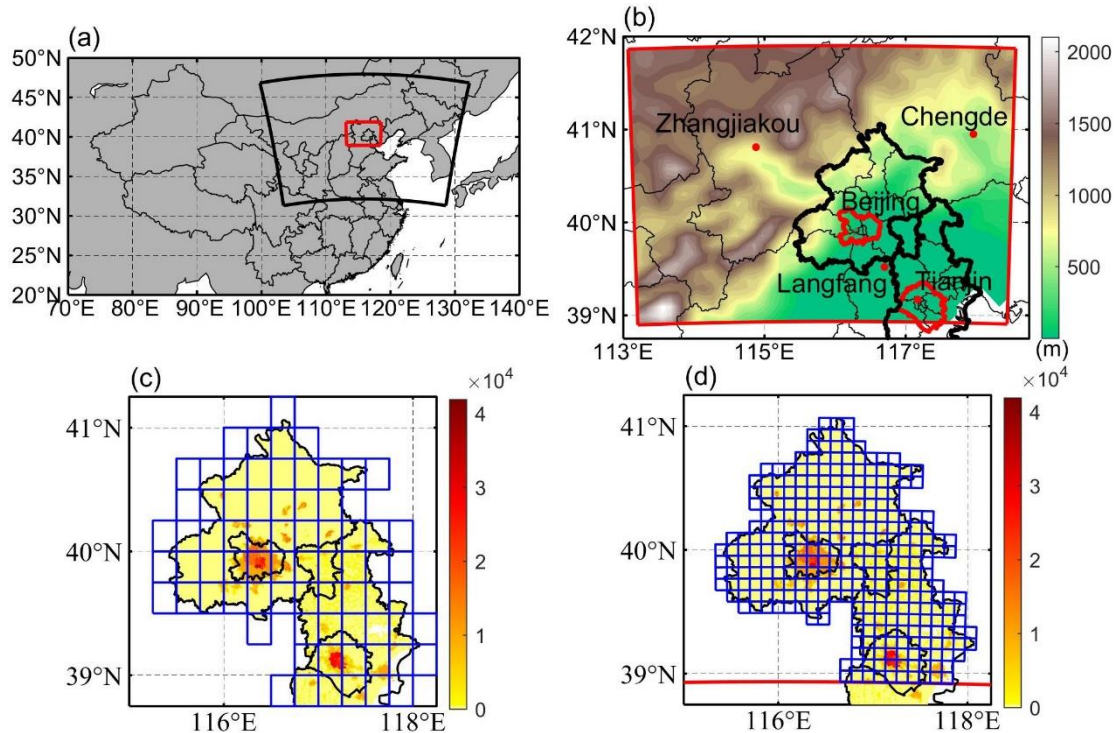
126 mountains on three sides, and a flat plain to the southeast coast (Fig. 1). Over the period
127 1971-2014, apparent temperature rose at a rate of $0.42^{\circ}\text{C}/10$ years over Beijing-Tianjin-
128 Hebei region, with urbanization having an effect of $0.12^{\circ}\text{C}/10$ years (Luo and Lau,
129 2021). By the end of 2019, the permanent resident population in Beijing exceeded 21
130 million. Tianjin, 100 km from Beijing, is the fourth largest city in China with a
131 population of about 15 million, and Langfang (population 4 million) is about 50 km
132 from Beijing. Thus, the region contains a comparable urbanized population as the
133 northeast US megalopolis. Since its climate is characterized by hot and moist summer
134 monsoon conditions, the population is at an enhanced risk as urban heat island effects
135 lead to city temperatures warming faster than their rural counterparts.

136

137 There are large uncertainties in projecting $\text{PM}_{2.5}$ concentration in the future due to both
138 climate and industrial policies. Statistical methods are much faster than atmospheric
139 chemistry models (Mishra et al., 2015), and different scenarios are easy to implement.
140 We use a Multiple Linear Regression (MLR) model to establish the links between $\text{PM}_{2.5}$
141 concentration, meteorology and emissions (Upadhyay et al., 2018; Tong et al., 2018).
142 We project and compare the differences of $\text{PM}_{2.5}$ concentration under G4 and RCP4.5
143 scenarios, and between different $\text{PM}_{2.5}$ emission scenarios. Accurate meteorological
144 data are crucial in simulating future apparent temperatures and $\text{PM}_{2.5}$ because all ESM
145 suffer from bias, and this problem is especially egregious at small scales. A companion
146 paper (Wang et al., 2022) looked at differences between downscaling methods with the
147 same 4 Earth System Models (ESM), domain and scenarios as we use here.

148

149 In this paper, we use the downscaled data to explore the effect of SAI on apparent
150 temperature and $\text{PM}_{2.5}$ over the greater Beijing megalopolis. The paper is organized as
151 follows. The data and methods of calculating AP, AP thresholds, the $\text{PM}_{2.5}$ MLR model
152 and its validation are briefly described in Section 2. The results from present day
153 simulation and future projections on apparent temperature and $\text{PM}_{2.5}$ are given in
154 Section 3, along with their associated impact analyses. In Section 4 we discuss and
155 interpret the findings, and finally we conclude with a summary of the main implications
156 of the geoengineering impacts on these two important human health indices in Section
157 5.



158
 159 **Figure 1.** **a**, The 10 km WRF domain (red box) nested inside a 30 km resolution WRF domain (large
 160 black sector). **b**, The inner domain topography and major conurbations (red dots), with the urban areas
 161 of Beijing and Tianjin enclosed in red curves. Panels **c** and **d** show the population density (persons per
 162 km²) of Beijing and Tianjin provinces (defined by black borders) in 2010 and the grid cells within the
 163 Beijing-Tianjin province (blue boxes) when downscaled by ISIMIP (**c**) and WRF (**d**).

164 2. Data and Methods

165 2.1 Scenarios, ESM, downscaling methods and bias correction

166 The scenarios, ESM, downscaling methods and bias correction methods we use here
 167 are as described in detail by Wang et al., (2022), and we just summarize the method
 168 briefly here. We use three different scenarios: RCP4.5 and RCP8.5 (Riahi et al., 2011)
 169 and the GeoMIP G4 scenario which span a useful range of climate scenarios: RCP4.5
 170 is similar (Vandyck et al., 2016) to the expected trajectory of emissions under the 2015
 171 Paris Climate Accord agreed Nationally Determined Contributions (NDCs); RCP8.5
 172 represents a formerly business-as-usual, no climate mitigation policies, large signal to
 173 noise ratio scenario; G4 represents a similar radiative forcing as produced by the 1991
 174 Mount Pinatubo volcanic eruption repeating every 4 years.

175
 176 Climate simulations are performed by 4 ESM: BNU-ESM (Ji et al., 2014), HadGEM2-
 177 ES (Collins et al., 2011), MIROC-ESM (Watanabe et al., 2011) and MIROC-ESM-
 178 CHEM (Watanabe et al., 2011). We compare dynamical and statistical downscaling
 179 methods to convert the ESM data to scales more suited to capturing differences between
 180 contrasting rural and urban environments. To validate the downscaled AP from model
 181 results, we use the daily temperature, humidity and wind speed during 2008-2017 from
 182 the gridded observational dataset CN05.1 with the resolution of $0.25^\circ \times 0.25^\circ$ based on

183 the observational data from more than 2400 surface meteorological stations in China,
184 which are interpolated using the “anomaly approach” (Wu and Gao, 2013). This dataset
185 is widely used, and has good performance relative to other reanalysis datasets over
186 China (Zhou et al., 2016; Yang et al., 2019; Yang et al., 2023; Yang and Tang, 2023).
187 Dynamical downscaling for the 4 ESM datasets was done with WRFv.3.9.1 with a
188 parameter set used for urban China studies (Wang et al., 2012) in two nested domains
189 at 30 and 10 km resolution over 2 time slices (2008-2017 and 2060-2069). We corrected
190 the biases in WRF output using the quantile delta mapping method (QDM; Wilcke et
191 al., 2013) with ERA5 (Hersbach et al., 2018) to preserve the mean probability density
192 function of the output over the domain without degrading the WRF spatial pattern. All
193 WRF results presented are after QDM bias correction. Statistical downscaling was done
194 with the trend-preserving statistical bias-correction Inter-Sectoral Impact Model
195 Intercomparison Project (ISIMIP) method (Hempel et al., 2013) for the raw ESM output,
196 producing output matching the mean ERA5 observational data in the reference
197 historical period with the same spatial resolution, while allowing the individual ESM
198 trends in each variable to be preserved.

199

200 **2.2 PM_{2.5} concentration and emission data**

201 In China there were few PM_{2.5} monitoring stations before 2013 (Xue et al., 2021).
202 However, aerosol optical depths produced by the Moderate Resolution Imaging
203 Spectroradiometer (MODIS) have been used to build a daily PM_{2.5} concentration
204 dataset (ChinaHighPM2.5) at 1 km resolution from 2000 to 2018 (Wei et al., 2020). We
205 use monthly PM_{2.5} concentration data during 2008-2015 from ChinaHighPM2.5 to train
206 the MLR model, and the data during 2016-2017 to validate it. Figure S1 shows annual
207 PM_{2.5} concentration over Beijing areas during 2008 (a) and 2017 (b).

208

209 Recent gridded monthly PM_{2.5} emission data were derived from the Hemispheric
210 Transport of Air Pollution (HTAP_V3) with a resolution of 0.1°×0.1° during 2008-2017,
211 which is a widely used anthropogenic emission dataset (Janssens-Maenhout et al.,
212 2015). PM_{2.5} emissions over Beijing areas during 2008 (c) and 2017 (d) are shown in
213 Fig. S1.

214

215 Future gridded monthly PM_{2.5} emissions to 2050 are available in the ECLIPSE V6b
216 database (Stohl et al., 2015), generated by the GAINS (Greenhouse gas Air pollution
217 Interactions and Synergies) model (Klimont et al., 2017). The ECLIPSE V6b baseline
218 emission scenario assumes that future anthropogenic emissions are consistent with
219 those under current environmental policies, hence it is the “worst” scenario without
220 considering any mitigation measures (Li et al., 2018; Nguyen et al., 2020). Projected
221 emissions are shown in Fig S2, with emissions plateauing at ~40 kt/year after 2030, so
222 we assume 2060s levels are similar. These ECLIPSE projections are significantly larger
223 than present day estimates from HTAP_V3. We therefore estimate 2060s emissions as
224 the recent gridded monthly PM_{2.5} emissions from HTAP_V3 scaled by the ratios of
225 2050 ECLIPSE emission to average annual emissions between 2010 and 2015. Before

226 processing data, PM_{2.5} concentration is bilinearly interpolated to the WRF and ISIMIP
227 grids, while PM_{2.5} emissions are conservatively interpolated to the target grids.
228

229 **2.3 Apparent temperature**

230 We used a widely used empirical formula to calculate the apparent temperature under
231 shade (Steadman 1984), that combines various meteorological fields, which also has
232 been widely used to study heat waves, heat stress and temperature-related mortality
233 (Perkins and Alexander, 2013; Lyon and Barnston, 2017; Lee and Sheridan, 2018; Zhu
234 et al., 2021):

$$235 \quad AP = -2.7 + 1.04 \times T + 2 \times P - 0.65 \times W \quad (1)$$

236 where AP is the apparent temperature (°C) under shade meaning that radiation is not
237 considered; T is the 2 m temperature (°C), W is the wind speed at 10 m above the ground
238 (m/s), and P is the vapor pressure (kPa) calculated by

$$239 \quad P = P_s \times RH \quad (2)$$

240 where P_s is the saturation vapor pressure (kPa), and RH is the relative humidity (%).
241 P_s is calculated using the Tetens empirical formula (Murray, 1966):

$$242 \quad P_s = \begin{cases} 0.61078 \times e^{\left(\frac{17.2693882 \times T}{T+237.3}\right)}, & T \geq 0 \\ 0.61078 \times e^{\left(\frac{21.8745584 \times (T-3)}{T+265.5}\right)}, & T < 0 \end{cases} \quad (3)$$

243 To assess the potential risks of heat-related exposure from apparent temperature, we
244 also count the number of days with $AP > 32^\circ\text{C}$ (NdAP_32) in the Beijing-Tianjin
245 province (Table S1). This threshold does not lead to extreme risk and death, instead it
246 is classified as requiring “extreme caution” by the US National Weather Service
247 (National Weather Service Weather Forecast Office,
248 <https://www.weather.gov/ama/heatindex>), but carries risks of heatstroke, cramps and
249 exhaustion. A threshold of 39°C is classed as “dangerous” and risks heatstroke. While
250 hotter AP thresholds would give a more direct estimate of health risks, the statistics of
251 these presently rare events mean that detecting differences between scenarios is less
252 reliable than using the cooler NdAP_32 threshold simply because the likelihood of rare
253 events are more difficult to accurately quantify than more common events that are
254 sampled more frequently. There is evidence that in some distributions, the likelihood
255 of extremes will increase more rapidly than central parts of a probability distribution,
256 for example large Atlantic hurricanes increasing faster than smaller ones (Grinsted et
257 al., 2013). But the conservative assumption is that similar differences between scenarios
258 would apply for higher thresholds as lower ones.

259 **2.4 Population Data Set**

260 Since health impacts scale with the number of people affected, we calculate the
261 NdAP_32 weighted by population (Fig. 1c and 1d). We employ gridded population data
262 (Fu et al., 2014; <https://doi.org/10.3974/geodb.2014.01.06.V1>) with a spatial resolution
263 of 1×1 km collected in 2010. The population density distribution in Beijing and Tianjin
264 provinces with the ISIMIP and WRF grid cells contained are shown in the Fig. 1c and
265 1d.

266

267 **2.5 MLR model calibration**

268 Many meteorological factors, such as temperature (You et al., 2017), precipitation (Guo
269 et al., 2016), wind speed (Yin et al., 2017), radiation (Chen et al., 2017), planetary
270 boundary layer height (Zheng et al., 2017) etc., can affect the $PM_{2.5}$ concentration. Their
271 relative importance differs regionally. But here we consider only differences that are
272 produced by the three scenarios, so for example we do not include precipitation in our
273 analysis because none of the ESM simulate significant changes in our domain (Table
274 S2). Previous studies have shown that wind and humidity are the dominant
275 meteorological variables for $PM_{2.5}$ concentration in region we study (Chen et al., 2020),
276 while changes in temperature and winds obviously impact local concentrations. Hence,
277 we generate an MLR model between $PM_{2.5}$ and temperature (T), relative humidity (H),
278 zonal wind (U), meridional wind (V) and $PM_{2.5}$ emissions (E) at every grid cell as
279 follows:

280

$$281 \quad PM_{2.5} = \sum a_i X_i + b \quad (4)$$

282 Where $X_{i(i=1,2,3,4,5)}$ are the five factors, a_i are the regression coefficients of the X_i
283 with $PM_{2.5}$, and b is the intercept, which is a constant. We assume that all factors
284 should be included in the regression. All the meteorological variables are from the
285 statistical and dynamical downscaling and bias corrected results during 2008-2017,
286 with the first 8 years used for training model and the second 2 years used for validating
287 model. We train the MLR for the 4 ESMs under statistical and dynamical downscaling
288 in each grid cell separately, thus accounting spatial differences in the weighting of the
289 X_i across the domain. Meteorological variables under G4, RCP4.5 and RCP8.5 during
290 2060-2069 are used for projection.

291

292 Here, we use $PM_{2.5}$ concentration including both primary and secondary $PM_{2.5}$ as the
293 dependent variable and primary $PM_{2.5}$ emission and meteorological factors as
294 independent variables in the MLR. Future $PM_{2.5}$ emissions will change in ways that are
295 rather speculative as they depend on technological innovation and policies that are
296 inherently unpredictable. The MLR assumes that the past emissions mix and secondary
297 aerosols remain unchanged in the future, but meteorological factors will also indirectly
298 impact secondary $PM_{2.5}$ to some extent.

299

300 The contributions of meteorology and $PM_{2.5}$ emissions on future concentrations are
301 examined by using recent $PM_{2.5}$ emissions (baseline) and future $PM_{2.5}$ emissions
302 (mitigation), and the downscaled climate scenarios. Modeled $PM_{2.5}$ concentration using
303 recent meteorology and $PM_{2.5}$ emissions during 2008-2017 (2010s) is considered as our
304 reference.

305

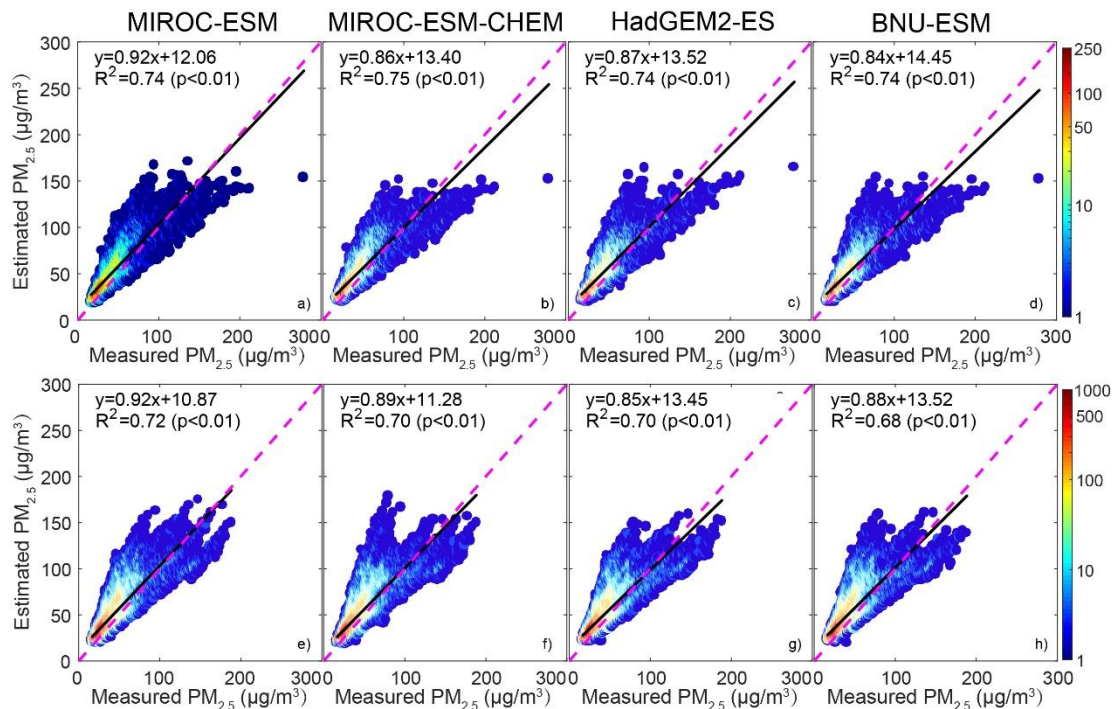
306 Collinearity of variables is inevitable in our domain. The domination of the seasonal
307 winter and summer monsoonal weather patterns mean that temperatures, precipitation

308 and wind direction are all highly seasonal and correlated. In winter, precipitation is
 309 minimal and northerly winds predominate, in summer the opposite is true. These three
 310 meteorological fields are important and also important for emissions, since sources are
 311 essentially absent from the north, while temperature and humidity dominate aerosol
 312 microphysics.

313

314 We use the variance inflation factor (VIF) to test if there is excessive collinearity in our
 315 MLR models. Generally, if VIF value is greater than 10, there is collinearity problem
 316 between variables. Figure S3 shows that there are indeed collinearity problems in some
 317 areas, but not in Beijing-Tianjin province, so there is no impact on the results for the
 318 urban areas. We explored the impact of collinearity on the results in high VIF grid cells
 319 by removing factors with VIF greater than 10 and the full variables model (Fig. S4 and
 320 Fig. S5). Using ISIMIP downscaling, we only removed the temperature, while we
 321 removed the temperature and U-wind in the WRF method. PM_{2.5} concentrations
 322 increased by ~1 μg/m² in all ESMS under G4 with the “baseline” scenario (Fig. S4), in
 323 contrast, PM_{2.5} concentrations decreased by 5-15 μg/m² with the “mitigation” scenario
 324 (Fig. S5) after dealing the collinearity problem. This means that PM_{2.5} concentration
 325 has more sensitivity to the PM_{2.5} emission after accounting for collinearity. Although
 326 the absolute PM_{2.5} concentrations are different accounting for collinearity, there are no
 327 significant differences in the changes of PM_{2.5} concentration between G4 and the
 328 2010s/RCP4.5/RCP8.5 in Beijing-Tianjin province.

329 2.6 MLR model validation



330

331 **Figure 2.** Scattergrams of PM_{2.5} concentration derived by MODIS and estimated by MLR during
 332 validation period (2016-2017). Top figures (a-d) are the ISIMIP statistical downscaling results, and
 333 bottom figures (e-h) are the WRF dynamical downscaling results. R² means the variance explained

334 by the MLR, and color bar denotes the density of datapoints at integer intervals.

335

336 Figure 2 shows the scattergram of PM_{2.5} concentration between ChinaHighPM2.5
337 dataset and MLR model during validation period based on ISIMIP and WRF results.
338 Observations and MLR models have Pearson's correlations coefficients around 0.86 for
339 ISIMIP results during the validation period, and the coefficient of determination of
340 MLRs are 0.74-0.75 (Fig. 2a-d). WRF Pearson's correlations are slightly lower, 0.82-
341 0.85, and explained variance ranges from 0.68-0.72 (Fig. 2e-h). These results are
342 similar as found by Jin et al. (2022). We also compare the spatial patterns of observed
343 and modeled PM_{2.5} in Fig. S6. Both ISIMIP and WRF results can simulate the
344 distribution characteristics of high concentration of PM_{2.5} in the southeast and low
345 concentration in the northwest.

346

347 We also tested the accuracy of our MLR model projection against simulations (Li et al.,
348 2023) with the Community Multiscale Air Quality (CMAQ) model developed by the
349 United States Environmental Protection Agency and which can simulate particulate
350 matter on local scales (Foley et al., 2010; Yang et al., 2019) when coupled to WRF. We
351 used the same meteorological forcing as Li with the "EIT1" PM_{2.5} emissions scenario
352 in 2050 under RCP4.5 (Fig.S7). The spatial patterns are well correlated in all seasons
353 (0.68-0.73), but PM_{2.5} concentrations are about twice as high in our MLR model as
354 from Li et al., (2023). PM_{2.5} concentrations from our regression model are also higher
355 than the referenced data during 2008-2017. While the difference in absolute PM_{2.5}
356 concentrations are significant, we mainly consider differences of PM_{2.5} concentration
357 between G4 and RCP4.5/RCP8.5 in our study which we cannot compare these
358 anomalies with the single RCP4.5 scenario simulated by Li et al. (2023). We do
359 compare the spatial pattern of differences in PM_{2.5} concentration between "base" and
360 "EIT1" under RCP4.5. Because of the small slope coefficient of PM_{2.5} emission in our
361 MLR, we do not capture the large reduction of PM_{2.5} concentration in the Beijing city
362 center seen by Li et al. (2023), (Fig. S8).

363

364 **2.7 Relative risks of mortality related to PM_{2.5}**

365 We estimate the effects of PM_{2.5} on mortality by considering changes in the relative risk
366 (RR) of mortality related to PM_{2.5}. We lack data on mortality rates in the study domain
367 without which we cannot estimate numbers of fatalities, just the average population-
368 weighted RR. Burnett et al. (2014) established the integrated exposure-response
369 functions we use. The RR is non-linear in concentration, that is an initially low PM_{2.5}
370 region will suffer higher mortality and RR than an initially high PM_{2.5} region if PM_{2.5}
371 is increased by the same amount. Ran et al. (2023) provide RR values for PM_{2.5}
372 concentrations up to 200 µg/m³ that includes the 5 main major disease endpoints
373 (Global Burden of Disease Collaborative Network, 2013) of PM_{2.5} related mortality:
374 chronic obstructive pulmonary disease, ischemic heart disease, lung cancer, lung
375 respiratory infection and stroke. We calculate the average population-weighted relative
376 risks based on the gridded population dataset (Section 2.4) and PM_{2.5} concentration in

377 the Beijing-Tianjin province defined in the Fig. 1c-1d, following Ran et al. (2023):

378
$$RR_{pop,k} = \frac{\sum_{g=1}^G POP_g \times RR_k(C_g)}{\sum_{g=1}^G POP_g} \quad (5)$$

379 $RR_{pop,k}$ is the average population-weighted relative risk of disease k ($k=1-5$), POP_g is
380 the population of grid g , and $RR_k(C_g)$ is the relative risk of disease k when $PM_{2.5}$
381 concentration is C_g in the grid of g .

382

383 **2.8 Determination of contributions to change in AP and $PM_{2.5}$**

384 Equation (1) describes how AP is calculated, and this can be broken down into how
385 much equivalent temperature is produced by each term (Fig. 3), with 2008-2017 as the
386 baseline interval for season-by-season contributors to AP. Across scenario seasonal
387 differences in contributors are then calculated as follows. We use an MLR approach,
388 since this minimizes the square differences from the mean across the dataset, with the
389 attendant assumption of independence between the data. Alternatives may also be
390 considered that e.g. minimize the impact of outliers by considering the magnitude of
391 the differences, but we prefer to keep the attractive properties of a least squares
392 approach. The dependent variable in the MLR is the change in AP (ΔAP) and the
393 independent variables are changes in each factor for each future scenario,

394
$$\Delta AP = \sum \alpha_i X_i + \beta \quad (6)$$

395 where $X_{i(i=1,2,3)}$ are the daily changes of the three meteorological factors between two
396 scenarios: 2 m temperature (ΔT), 2 m relative humidity (ΔRH) and 10 m wind speed
397 (ΔW), α_i are the regression coefficients of the X_i with ΔAP , and β is the intercept,
398 which is a constant. We assume that all three meteorological factors should be included
399 in the regression and we estimate the contributions of each factor to changes of AP as:

400
$$K_i = \frac{\alpha_i \bar{X}_i}{\sum \alpha_i \bar{X}_i} \quad (7)$$

401 where $K_{i(i=1,2,3)}$ is the contributions (in units of temperature) from each factor to the
402 changes of the AP, and \bar{X}_i are the mean differences in temperature equivalent due to
403 each factor between two scenarios.

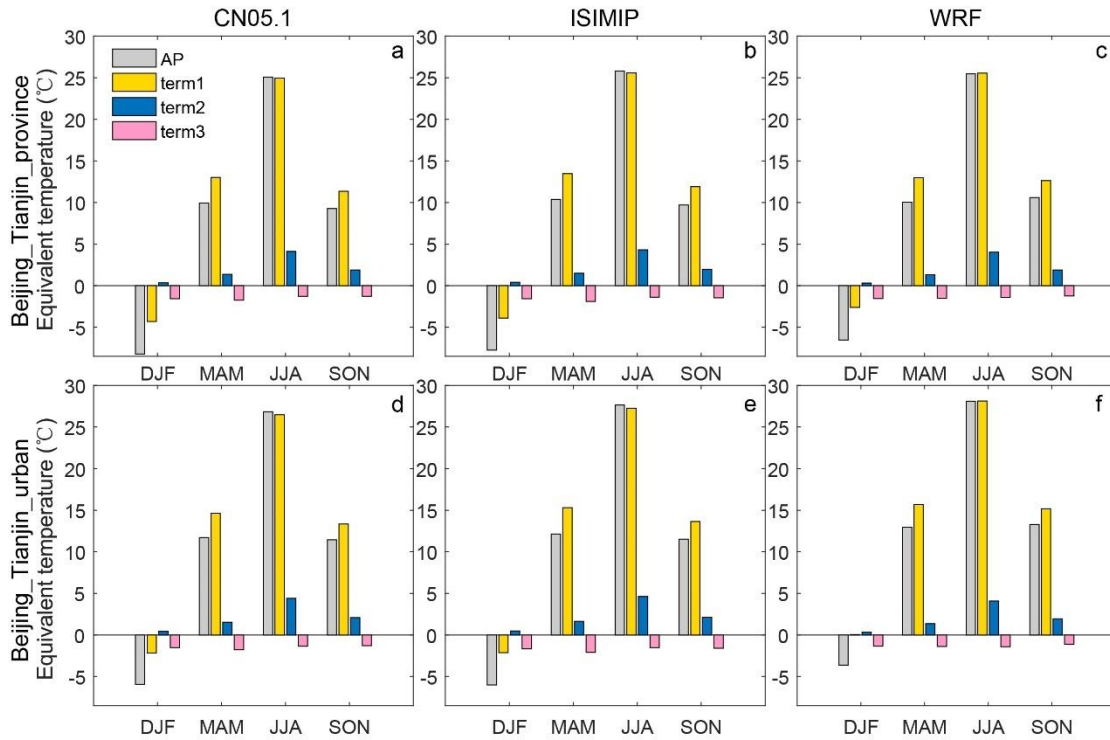
404

405 The contribution of changes in each factor in changes of $PM_{2.5}$ is simpler since we
406 assume that the relationship between each factor and $PM_{2.5}$ is linear, and so its
407 contribution is the ratio of product of the regression coefficient and the change of each
408 factor to the change of $PM_{2.5}$.

409

410 **3. Results**

411 **3.1 Recent apparent temperatures**



412

413

Figure 3. Seasonal averaged AP and equivalent temperature of each term in equation 1 for Beijing-Tianjin province (a-c) and Beijing-Tianjin urban areas (d-f) during 2008-2017 from CN05.1 (a, d), 4-model ensemble mean after ISIMIP (b, e) and ensemble mean after WRF (c, f). Term 1 is 1.04T, term 2 is 2P and term 3 is -0.65W.

416

417

418

419

420

421

422

423

424

425

426

427

428

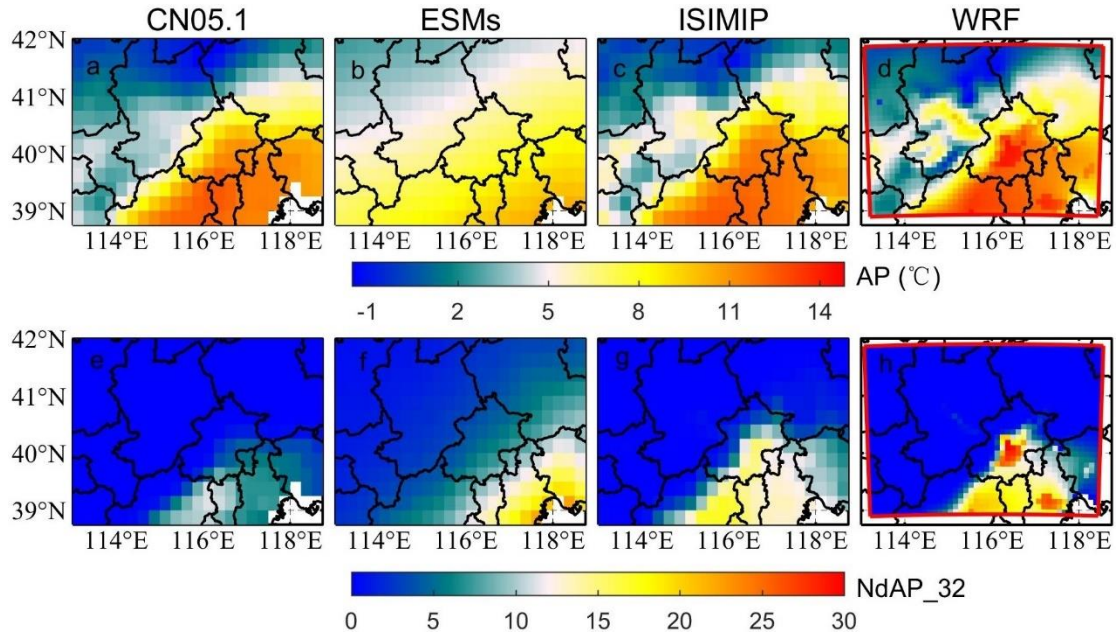
429

430

431

432

Figure 3 shows the seasonal averaged AP and equivalent temperatures caused by temperature, relative humidity and wind speed in Beijing-Tianjin province and Beijing-Tianjin urban areas during 2008-2017. According to the CN05.1 results (Fig. 3a, 3d), AP and the separate 3 terms show similar seasonal patterns over the whole province and just the urban areas. Vapor pressure is higher in summer and wind speed is higher in spring. AP is lower than 2 m temperature in all seasons except summer, and especially lower in winter. AP, temperature, vapor pressure and wind speed are all higher in urban areas than in the surrounding rural region in any season. The ISIMIP results (Fig. 3b, 3e), by design, perfectly reproduce the CN05.1 seasonal characteristics of AP, temperature, vapor pressure and wind speed. WRF shows a similar pattern with that from CN05.1, but for the Beijing-Tianjin province, WRF overestimates both 2 m temperature and AP in winter by 2.1°C and by 1.7°C respectively relative to CN05.1 (Fig. 3c). In the Beijing-Tianjin urban areas, WRF overestimates the temperature and AP relative to CN05.1 in all seasons, especially in winter (Fig. 3f).



433

434 **Figure 4.** Top row: the spatial distribution of mean apparent temperature from CN05.1 (a), raw ESMs
 435 ensemble mean after bilinear interpolation (b), 4-model ensemble mean after ISIMIP (c) and ensemble
 436 mean after WRF (d) during 2008-2017. Bottom row: the spatial distribution of annual mean number of
 437 days with AP > 32°C from CN05.1 (e), ESMs (f), ISIMIP (e) and WRF (f) during 2008-2017. Fig. S9
 438 and Fig. S10 show the pattern of AP and NdAP_32 for the individual ESM.

439 We compare the simulations of mean apparent temperature and NdAP_32 from both
 440 WRF dynamical downscaling with QDM and from ISIMIP statistical downscaling
 441 during 2008-2017 in Fig. 4. Both WRF with QDM and ISIMIP methods produce a
 442 pattern of apparent temperature which is close to that from CN05.1. While the raw AP
 443 from ESMs is overestimated in Zhangjiakou high mountains and underestimated in the
 444 southern plain, and shares a similar pattern with temperature from ESMs (Wang et al.,
 445 2022). The raw ESM outputs were improved after dynamical and statistical
 446 downscaling. The average annual AP from ISIMIP (9.6-9.7°C) is 0.5°C higher than that
 447 from CN05.1 (9.1°C) over the Beijing-Tianjin province for all ESMs (Table 1). While
 448 WRF produces warmer apparent temperatures in the city centers of Beijing and Tianjin
 449 and lower ones in the high Zhangjiakou mountains than recorded in the lower resolution
 450 CN05.1 observations. There are also differences between different models after WRF
 451 downscaling. For example, apparent temperatures from the two MIROC models
 452 downscaled by WRF are the warmest. In contrast AP from all 4 ESMs after ISIMIP
 453 shows very similar patterns (Fig. S9).

454

455 ESMs tend to overestimate the number of days with AP>32°C in southeastern Beijing
 456 and the whole Tianjin province. Both ISIMIP and WRF appear to overestimate the
 457 NdAP_32 in Beijing urban areas and the southerly lowland areas although NdAP_32 is
 458 close to zero in the colder rural areas at relatively high altitude for both downscaling
 459 methods. Some of these differences may be due to the WRF simulations being at finer
 460 resolution than the 0.25°× 0.25° CN05.1, leading to higher probabilities of high AP in
 461 urban areas (Fig. 5d). ISIMIP results also show slight overestimations, especially in the

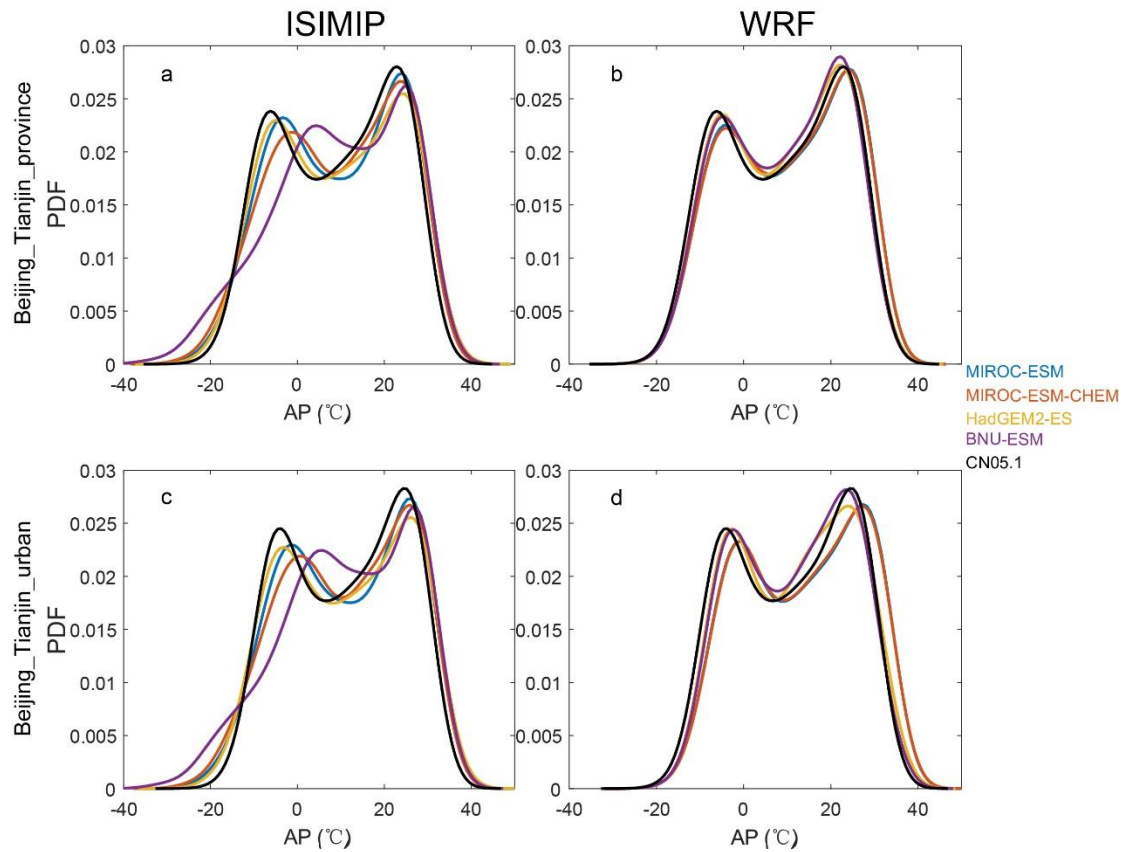
462 tails of the distribution ($AP > 30^{\circ}\text{C}$) for urban areas (Fig. 5c). CN05.1 gives about 5
 463 NdAP_32 per year in southern Beijing and Tianjin, but there are nearly 15 NdAP_32
 464 from ISIMIP, and over 20 NdAP_32 per year from WRF downscaling in the Beijing-
 465 Tianjin urban areas during 2008-2017. NdAP_32 from WRF and ISIMIP downscaling
 466 of all ESM is overestimated relative to CN05.1. But there are differences in ESM under
 467 the two downscalings: with ISIMIP, HadGEM2-ES and BNU-ESM have more
 468 NdAP_32 than the two MIROC models, while the reverse occurs with WRF (Fig. S10).
 469

470 **Table 1.** The annual mean apparent temperature and population weighted NdAP_32 in Beijing-Tianjin
 471 province and Beijing-Tianjin urban areas (Fig. 1b) from CN05.1, ISIMIP and WRF during 2008-2017.

Data Sources	AP ($^{\circ}\text{C}$)				NdAP_32 (day yr $^{-1}$)	
	Provinces		Urban		Population weighted for province (Fig. 1c, 1d)	
	WRF	ISIMIP	WRF	ISIMIP	WRF	ISIMIP
MIROC-ESM	10.5	9.6	13.6	11.4	22.2	10.1
MIROC-ESM-CHEM	10.5	9.6	13.6	11.4	21.9	11.0
HadGEM2-ES	9.5	9.6	12.0	11.4	12.3	11.1
BNU-ESM	9.4	9.7	11.8	11.5	10.2	12.7
CN05.1	9.1		11.1		2.4	

472 The Taylor diagram of the daily mean apparent temperature in Beijing-Tianjin province
 473 and Beijing-Tianjin urban areas from 2008-2017 for the 4 ESMs shows that correlation
 474 coefficients between ESMs and CN05.1 are greater than 0.85 under both downscaling
 475 methods. Although there are differences between ESMs, the performance of WRF, with
 476 higher correlation coefficient and smaller SD (standard deviation) and RMSD (root
 477 mean standard deviation), is usually superior to ISIMIP (Fig. S11). Taking the Beijing-
 478 Tianjin urban areas as an example (Fig. S11b), under the ISIMIP method, MIROC-
 479 ESM, MIROC-ESM-CHEM and HadGEM2-ES have the same correlation coefficient
 480 (0.92) and RMSD (5.4°C) with the CN05.1, while BNU-ESM has lower correlation
 481 coefficient (0.88) and higher RMSD (7.0°C). Under WRF simulations, MIROC-ESM
 482 and MIROC-ESM-CHEM have larger correlation coefficients and smaller RMSD with
 483 CN05.1 than HadGEM2-ES and BNU-ESM.

484 Figure 5 shows the probability density functions (pdf) of daily AP from the four ESMs
 485 under ISIMIP and WRF in Beijing-Tianjin province and Beijing-Tianjin urban areas
 486 during 2008-2017. ISIMIP overestimates the probability of extreme cold AP relative to
 487 CN05.1 (especially BNU-ESM), although all ESM reproduce the CN05.1 pdf well at
 488 high AP. WRF can reproduce the CN05.1 distribution of AP better than ISIMIP, but
 489 high AP is overestimated relative to CN05.1 and the urban areas perform less well than
 490 the whole Beijing-Tianjin province. In urban areas all ESMs driving WRF tend to
 491 underestimate the probability of lower AP and to overestimate the probability of higher
 492 AP, especially the two MIROC models (Fig. 5d). Fig. S12 displays the annual cycle of
 493 monthly AP, with ISIMIP proving excellent by design, at reproducing the monthly AP.
 494 While under WRF downscaling AP shows more across model differences, especially
 495 during summer and with greater spread for the urban areas.

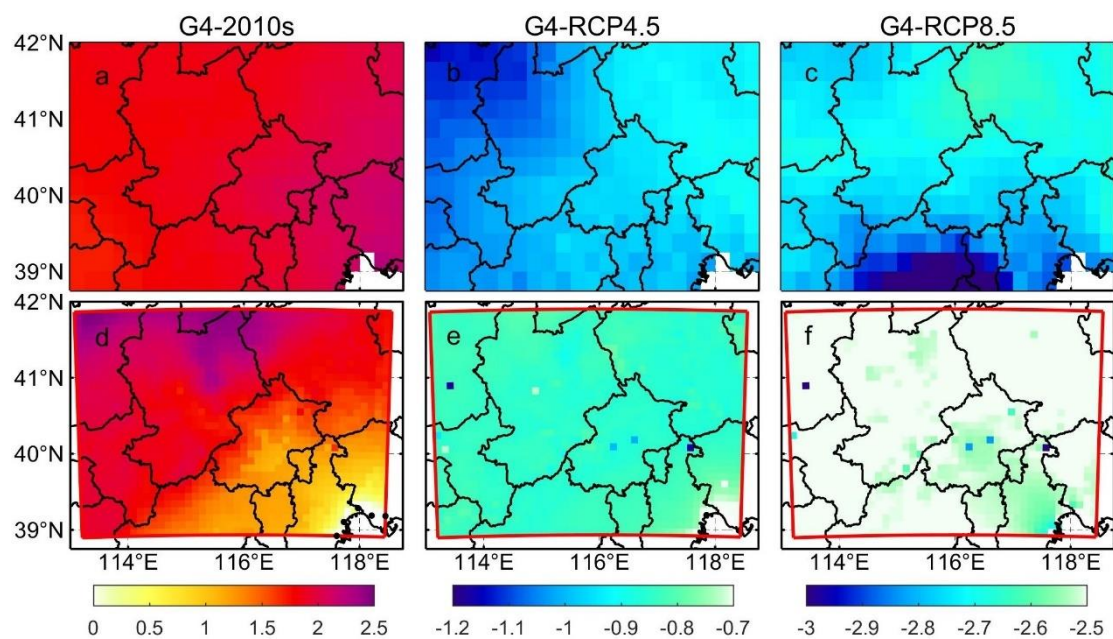


496

497 **Figure 5.** The probability density function (pdf) for daily apparent temperature under ISIMIP (a, c) and
 498 WRF (b, d) results in Beijing-Tianjin province (a, b) and Beijing-Tianjin urban areas (c, d) during 2008-
 499 2017.

500 3.2 2060s apparent temperatures

501 3.2.1 Changes of apparent temperature



502

503 **Figure 6.** Spatial pattern of ensemble mean apparent temperature difference (°C) under different
504 scenarios over 2060-2069: G4-2010s (left column), G4-RCP4.5 (middle column) and G4-RCP8.5 (right
505 column) based on ISIMIP and WRF methods. 2010s refers to the 2008-2017 period. Stippling indicates
506 grid points where differences or changes are not significant at the 5% level according to the Wilcoxon
507 signed rank test.

508

509 Figure 6 shows the ISIMIP and WRF ensemble mean changes in the annual mean AP
510 under G4 during 2060-2069 relative to the past and the two future RCP scenarios.
511 ISIMIP-downscaled AP (Fig. 6a-6c) shows significant anomalies ($p < 0.05$), with whole
512 domain rises of 2.0 °C in G4-2010s, and falls of 1.0 °C and 2.8 °C in G4-RCP4.5 and
513 G4-RCP8.5 respectively. In WRF results, AP under G4 is about 1-2 °C warmer than
514 that under 2010s, 0.8 °C and 2.5 °C colder than that under RCP4.5 and RCP8.5 over
515 the whole domain. Individual ESM results downscaled by ISIMIP and WRF are in Fig.
516 S14 and Fig. S15. For both ISIMIP and WRF downscaling results, the two MIROC
517 models show stronger warming than the other two models between G4 and the 2010s.
518 WRF-downscaled AP driven by HadGEM2-ES exhibits the strongest cooling, with
519 decreases of 1.7 °C between G4 and RCP4.5 and falls of 3.0 °C between G4 and RCP8.5.
520 Although different ESMs show different changes in AP between G4 and other scenarios,
521 changes in AP are almost the same everywhere for a given ESM in the ISIMIP results
522 (Fig. S14). WRF-downscaled AP anomalies driven by two MIROC models are larger
523 in the Zhangjiakou mountains and smaller in the Beijing urban areas and Tianjin city
524 between G4 and 2010s (Fig. S15). Changes in AP from ISIMIP results, whether across
525 whole province or just the urban areas, are statistically identical given scenarios (Table
526 2), which is consistent with patterns in figure 6. AP under G4 is 0.8 °C (1.0 °C) and
527 2.6 °C (2.8 °C) colder than that under RCP4.5 and RCP8.5 in Beijing-Tianjin urban
528 areas from ISIMIP (WRF) results. The warming between G4 and 2010s in urban areas
529 is 1.0 °C in WRF results, while that is 2.0 °C in ISIMIP results (Table 2).

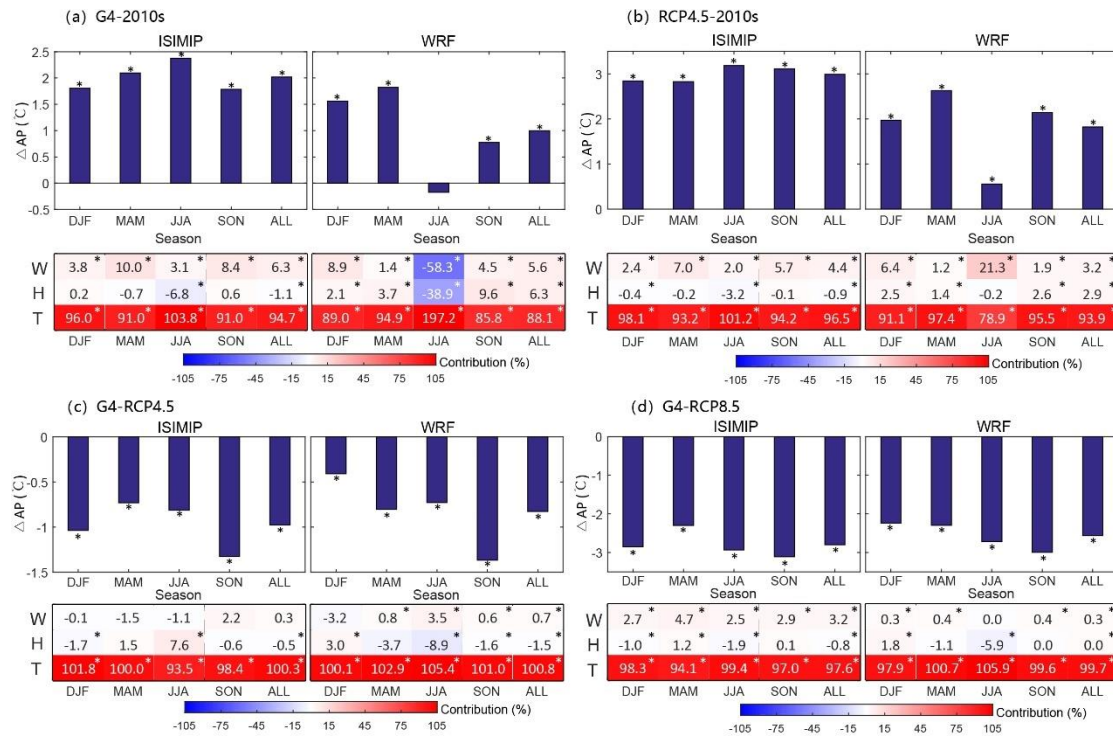
530

531 **Table 2.** Difference of apparent temperature between the G4 and other scenarios for the Beijing-Tianjin
532 province and Beijing-Tianjin urban areas as defined in Fig. 1b during 2060-2069. Bold indicates the
533 differences or changes are significant at the 5% level according to the Wilcoxon signed rank test.
534 (Units: °C)

Model	G4-2010s				G4-RCP4.5				G4-RCP8.5			
	WRF		ISIMIP		WRF		ISIMIP		WRF		ISIMIP	
	Urban	Province	Urban	Province	Urban	Province	Urban	Province	Urban	Province	Urban	Province
MIROC-ESM	0.9	1.5	2.2	2.2	-0.5	-0.4	-0.9	-0.9	-2.3	-2.1	-2.8	-2.7
MIROC-ESM-CHEM	0.9	1.5	2.9	2.8	-0.4	-0.4	-0.1	-0.1	-2.0	-2.0	-2.1	-2.1
HadGEM2-ES	1.1	1.0	1.8	1.7	-1.6	-1.6	-1.6	-1.6	-3.1	-3.1	-3.3	-3.3
BNU-ESM	1.2	1.1	1.2	1.3	-0.8	-0.8	-1.3	-1.3	-2.8	-2.7	-2.9	-2.9
Ensemble	1.0	1.3	2.0	2.0	-0.8	-0.8	-1.0	-1.0	-2.6	-2.5	-2.8	-2.8

535

536 3.2.2 Contributing factors to changes in AP



537

538 **Figure 7.** The seasonal changes of AP (ΔAP) and the seasonal contribution of climatic factors to ΔAP
 539 for Beijing and Tianjin urban areas under ISIMIP and WRF between G4 and 2010s **(a)**, G4 and 2010s
 540 **(b)**, G4 and RCP4.5 **(c)** and G4 and RCP8.5 **(d)** in the 2060s based on ensemble mean results. Colors
 541 and numbers in each cell correspond to color bar, and “*” above the columns and in the cells indicate
 542 differences are significant at the 5% significant level under the Wilcoxon test.

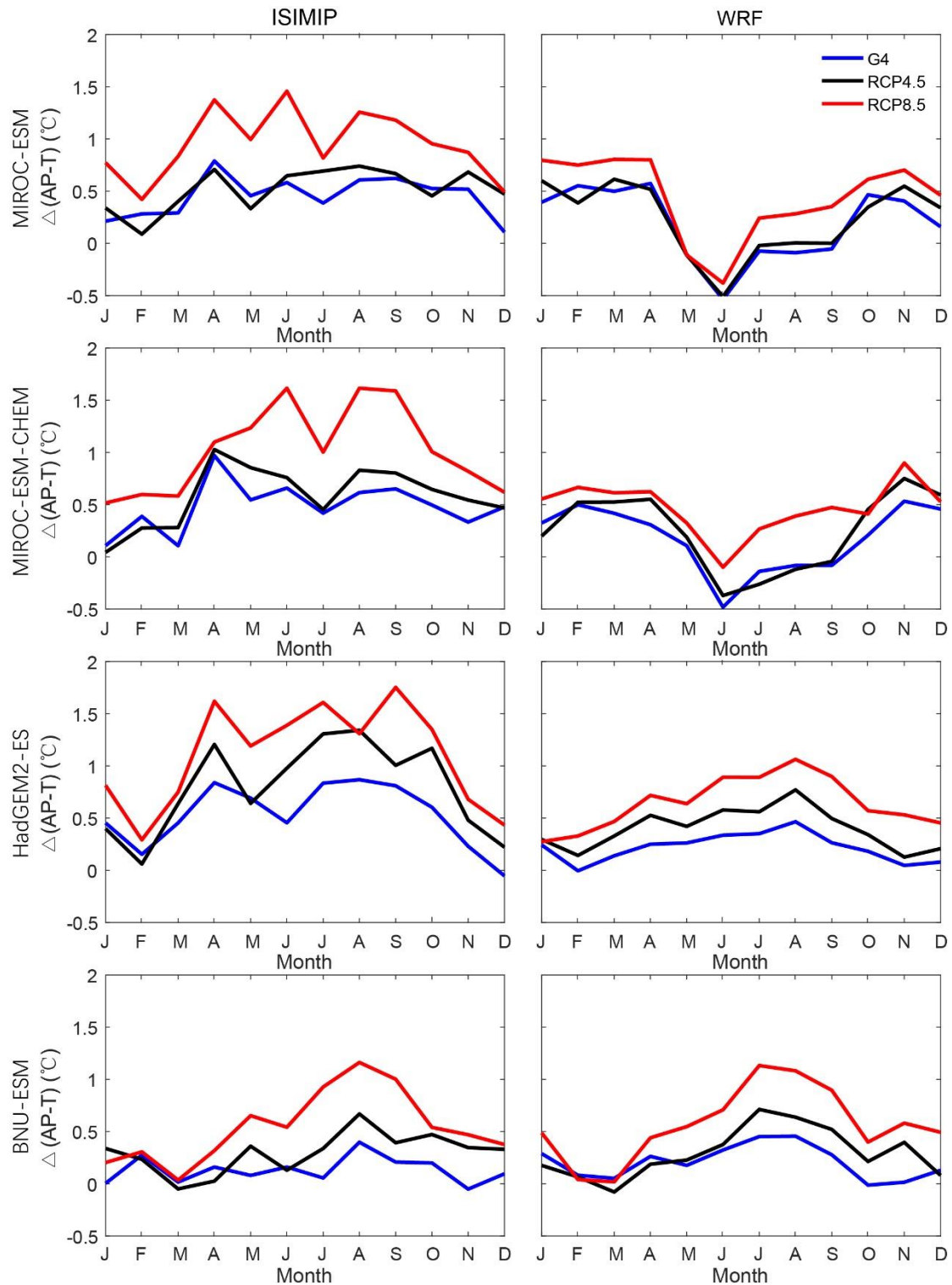
543

544 Figure 7 shows the ISIMIP and WRF ensemble mean changes in the annual mean AP
 545 anomalies G4 during 2060-2069 relative to the past and the two future RCP scenarios.
 546 ISIMIP-downscaled AP (Fig. 7a-7c) shows significant anomalies ($p < 0.05$) across the
 547 whole domain, even for the relatively small differences in G4-RCP4.5. ΔAP by WRF
 548 is lower than that by ISIMIP. Between G4 and 2010s, AP are projected to have increases
 549 of 1.8 (1.6), 2.1 (1.8), 2.4 (-0.2), 1.8 (0.8) °C from winter to autumn in ISIMIP (WRF)
 550 results. In ISIMIP results, the contribution of temperature ranges from 91%-104%, and
 551 the contribution of wind speed ranges from 3%-10% in all seasons, while the
 552 contribution of humidity is negative or insignificant (Fig. 7a). However, the
 553 contribution of humidity is positive in WRF results (Fig. 7a). Between RCP4.5 and
 554 2010s, annual mean AP is projected to increase by 3.0 °C and 1.8 °C in ISIMIP and
 555 WRF results respectively, which is higher than that between G4 and 2010s. The increase
 556 of temperature and decrease of wind speed have a significant impact on the annual
 557 average ΔAP contributed 97% (94%) and 4% (3%) in ISIMIP (WRF) results. The
 558 contributions of changes in humidity are significantly positive under G4 and RCP4.5 in
 559 WRF results, while it is the opposite in the ISIMIP results (Fig. 7a-7b).

560

561 Relative to RCP4.5 in the 2060s, AP is projected to decrease by 1.0 (0.4), 0.7 (0.8), 0.8
 562 (0.7), and 1.3 (1.4) °C from winter to autumn under G4 in ISIMIP (WRF) results (Fig.
 563 7c). In summer, the contribution from changes in temperature and humidity are 94%

564 (105%) and 8% (-9%) in ISIMIP (WRF) results, respectively. There are insignificant
 565 contributions from wind speed under ISIMIP results, but a significant slight positive
 566 contribution (0.7%-4%) under WRF results (Fig. 7c). The annual mean AP under G4 is
 567 2.8 (2.6) °C lower than that under RCP8.5 in ISIMIP (WRF) result. In this case, the
 568 contribution of changes in wind on ΔAP ranges from 3%-5% by ISIMIP, while it is
 569 close to 0 by WRF. As expected, ΔAP is mainly determined by the changes in
 570 temperature, with contributions usually above 90% between different scenarios.



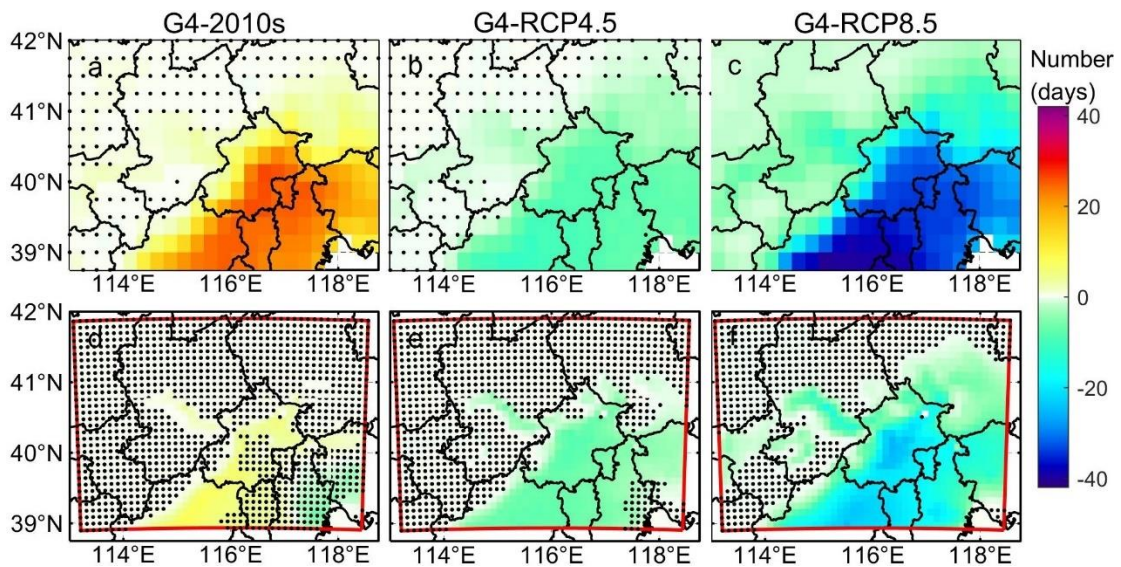
571

572 **Figure 8.** The change of apparent temperature based on air temperature under three scenarios (G4,
 573 RCP4.5 and RCP8.5) in four ESMs under ISIMIP (left column) and WRF (right column) for urban areas
 574 relative to the 2010s.

575

576 A useful measure of heat impacts that may be missed if considering only at air
 577 temperatures is the seasonality of the differences between AP and air temperature
 578 ($\Delta(\text{AP-T})$; Fig. 8). The four model ensemble annual mean $\Delta(\text{AP-T})$ under ISIMIP is
 579 projected to rise by 0.4°C, 0.5°C and 0.9°C under G4, RCP4.5 and RCP8.5, relative to
 580 the 2010s. Under WRF, $\Delta(\text{AP-T})$ is much smaller than under ISIMIP but still rising
 581 faster than air temperatures: by 0.2°C, 0.3°C and 0.5°C under G4, RCP4.5 and RCP8.5
 582 relative to the 2010s, respectively. In general, the largest anomalies in $\Delta(\text{AP-T})$ are in
 583 summer under both WRF and ISMIP downscaling, but the two MIROC models under
 584 WRF have small or even negative $\Delta(\text{AP-T})$ in summer with WRF.

585 3.2.3 Changes of the number of days with AP>32°C



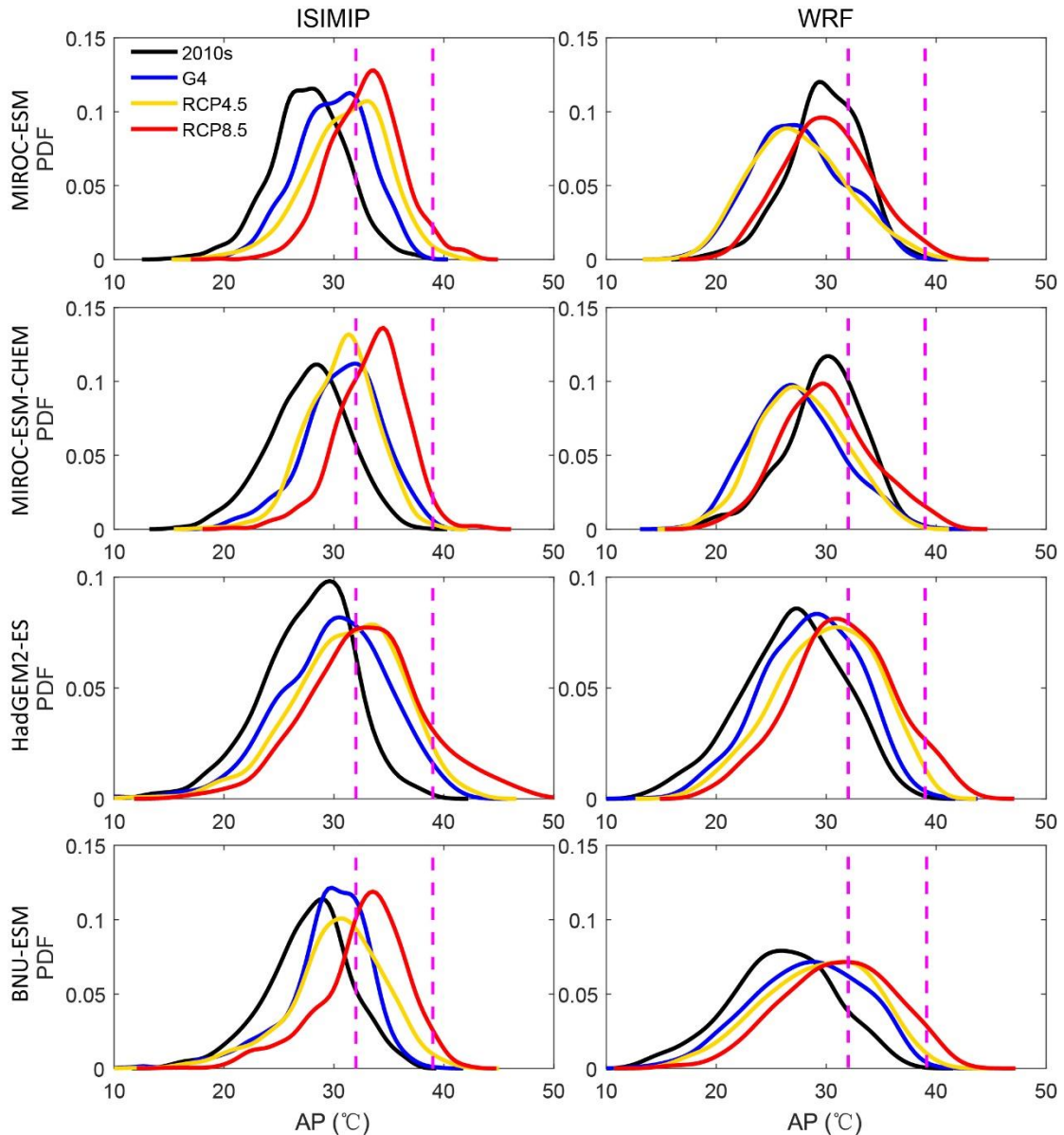
586

587 **Figure 9.** Ensemble mean differences in annual number of days with AP > 32°C (NdAP_32) between
 588 scenarios for 2060-2069: G4-2010s (left column), G4-RCP4.5 (second column) and G4-RCP8.5 (right
 589 column) based on ISIMIP method and WRF. 2010s means the results simulated during 2008-2017.
 590 Stippling indicates grid points where differences or changes are not significant at the 5% level according
 591 to the Wilcoxon signed rank test. Corresponding ISIMIP results for each ESM are in Fig. S16, and WRF
 592 results in Fig. S17.

593

594 The NdAP_32 anomalies in Figure 9 show that ISIMIP projects an increase of about 20
 595 days per year with AP>32 °C for the southeast of Beijing province and 10 days in the
 596 western areas of Beijing under G4 relative to the 2010s. NdAP_32 is about 10 days
 597 fewer under G4 than RCP4.5 with no clear spatial differences. G4 has about 35 fewer
 598 NdAP_32 days in the southern part of the domain and 20 fewer days in the western
 599 domain than the RCP8.5 scenario. In contrast WRF suggests that most areas do not
 600 show any significant difference between G4 and the 2010s, while the anomalies relative
 601 to RCP4.5 are similar as ISIMIP, the differences are insignificant over more area than

602 ISIMIP. G4-RCP8.5 anomalies with WRF are smaller than with ISIMIP, and differences
 603 are not significant in the Zhangjiakou high mountains. The urban areas show larger
 604 decreases in NdAP_32 than the more rural areas, even in the low altitude plain.
 605 Individual ESM show almost no statistically significant differences between G4 and
 606 RCP4.5 (Fig. S16 and S17), but the differences seen in Fig. 9 are significant because of
 607 the larger sample size in the significance test. All ESMs with ISIMIP show more
 608 NdAP_32 in the urban areas under G4 than the 2010s, while two MIROC models
 609 driving WRF show fewer NdAP_32 in Beijing-Tianjin urban areas (Fig. S16, S17).
 610



611
 612 **Figure 10.** Probability density distributions of daily apparent temperature (AP) in summer (JJA) over
 613 Beijing-Tianjin urban areas under recent period (2008-2017), and the 2060s under G4, RCP4.5 and
 614 RCP8.5 scenarios from ISIMIP and WRF results. The purple dotted lines are at AP of 32°C and 39°C.
 615

616 The pdf of daily apparent temperature in summer over Beijing-Tianjin urban areas (Fig.
 617 10) shifts rightwards for G4, RCP4.5 and RCP8.5 during the 2060s relative to the 2010s.

618 Figure 10 shows that by the 2060s, the dangerous threshold of $AP > 39$ is crossed
 619 frequently under RCP8.5 with both WRF and ISIMIP downscaling, but for the RCP4.5
 620 and G4 scenarios these events are much rarer. ISIMIP results tend to show higher
 621 probability tails (extreme events) than under WRF simulations.

622

623 Population weighted $NdAP_{32}$ in the 2060s for Beijing-Tianjin province is shown in
 624 Table 3. ISIMIP downscaling suggests ensemble mean rises in $NdAP_{32}$ of 22.4 days
 625 per year under G4 relative to the 2010s, but that G4 has 8.6 and 33.5 days per year
 626 fewer than RCP4.5 and RCP8.5, respectively. $NdAP_{32}$ from WRF under G4 is
 627 reduced by 19.6 days per year relative to RCP8.5, and by 6.3 days relative to RCP4.5
 628 (Table 3).

629

630 **Table 3.** Difference of population weighted $NdAP_{32}$ between the G4 and other scenarios for Beijing-
 631 Tianjin province (Fig. 1c, 1d) during 2060-2069. Bold indicates the changes are significant at the 5%
 632 level according to the Wilcoxon signed rank test. (Units: day y^{-1}).

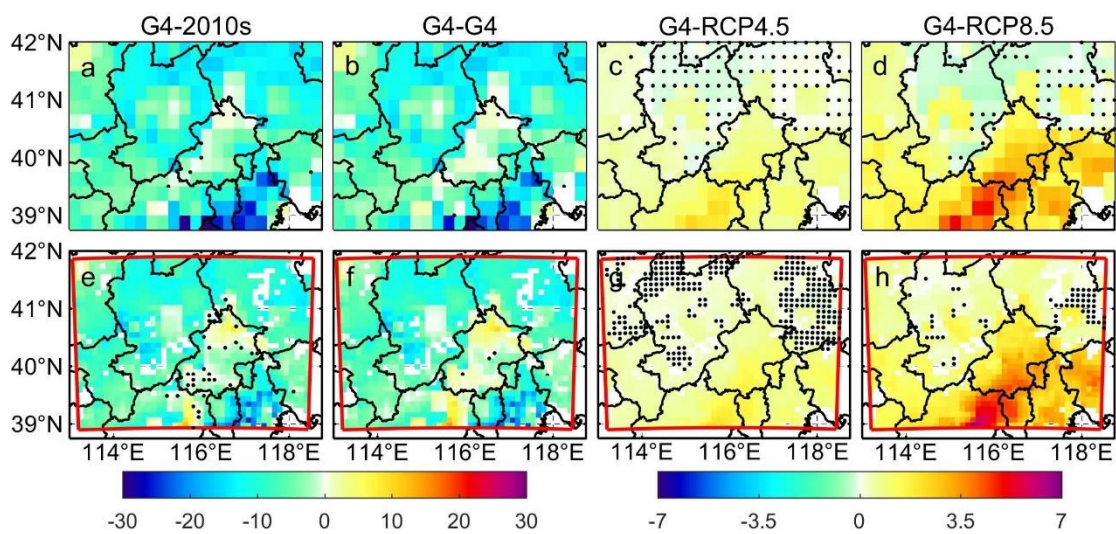
633

Beijing-Tianjin province	G4-2010s		G4-RCP4.5		G4-RCP8.5	
	ISIMIP	WRF	ISIMIP	WRF	ISIMIP	WRF
MIROC-ESM	18.6	-8.1	-17.0	0.8	-35.4	-13.1
MIROC-ESM-CHEM	28.7	-10.2	3.9	-2.2	-33.7	-15.5
HadGEM2-ES	25.7	9.4	-12.5	-13.5	-24.3	-25.3
BNU-ESM	16.4	13.6	-8.6	-10.4	-40.5	-24.4
Ensemble	22.4±2.9	1.2±6.0	-8.6±4.5	-6.3±3.4	-33.5±3.4	-19.6±3.1

634

635 3.3 $PM_{2.5}$ in the 2060s

636 3.3.1 $PM_{2.5}$ scenarios in the 2060s



637

638 **Figure 11.** Spatial patterns of ensemble mean $PM_{2.5}$ concentration difference ($\mu\text{g}/\text{m}^3$) between
 639 “mitigation” under G4 in the 2060s and reference (a, e), between “mitigation” and “baseline” under
 640 G4 in the 2060s (b, f), between G4 and RCP4.5 under “mitigation” scenario in the 2060s (c, g), and

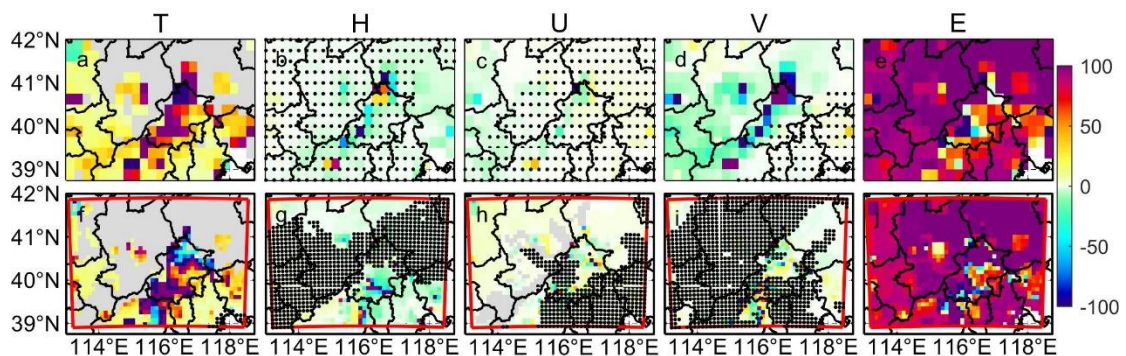
641 between G4 and RCP8.5 under “mitigation” scenario in the 2060s (**d, h**) based on ISIMIP (**a-d**) and
 642 WRF (**e-h**) results. Excessive collinearity variables have been removed (Fig. S18 shows the results
 643 without this procedure). Stippling indicates grid points where differences or changes are not
 644 significant at the 5% significant level according to the Wilcoxon signed rank test.

645

646 We firstly project the change of PM_{2.5} under G4 and the aerosol mitigation scenario in
 647 2060s relative to 2010s (Fig. 11a, e). Both ISIMIP and WRF project PM_{2.5} decreases in
 648 most areas, especially in Tianjin and Langfang, but PM_{2.5} decreases more under ISIMIP
 649 than WRF. PM_{2.5} concentration decreases by 7.6 μg/m³ over Beijing-Tianjin province
 650 in ISIMIP, and decrease by 5.4 μg/m³ in WRF (Table S3). PM_{2.5} concentration is 0.5-8
 651 μg/m³ higher in northern Beijing under G4 (“mitigation”) than that during the 2010s in
 652 WRF. To show the impact of emission reductions, we compare the PM_{2.5} concentration
 653 between aerosol “baseline” and “mitigation” scenarios under G4 in the 2060s (Fig. 11b,
 654 11f), and compare the “mitigation” PM_{2.5} concentration under G4 and the RCP
 655 scenarios in the 2060s to clarify the effect of geoengineering compared with climate
 656 warming. Compared with “baseline” scenario, PM_{2.5} concentration is less under
 657 “mitigation” scenario as expected in both ISIMIP and WRF under G4 (Fig. 11b, 11f),
 658 and has a similar spatial pattern with that in Fig. 11a and 11e. Compared with RCP4.5
 659 and RCP8.5, PM_{2.5} concentration under G4 are higher over the Beijing-Tianjin province
 660 in ISIMIP results (Fig. 11c-11d), but with large differences between the 4 ESMs. G4
 661 PM_{2.5} is simulated greater than in RCP scenarios under HadGEM2-ES and BNU-ESM
 662 (Fig. S19k, l, o, p), but there are insignificant differences in most areas under the two
 663 MIROC models (Fig. S19c, d, g, h). PM_{2.5} concentrations are larger between G4 and
 664 RCP8.5. WRF simulations shows similar changes in PM_{2.5} between G4 and RCPs as
 665 ISIMIP over Beijing-Tianjin province (Fig. 11g-h).

666

667 3.3.2 PM_{2.5} meteorological and emissions controls in the 2060s



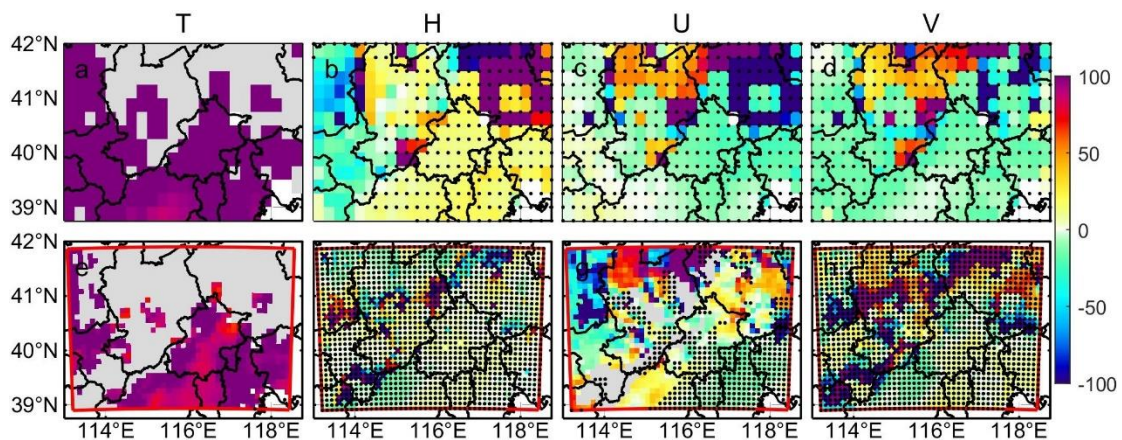
668

669 **Figure 12.** Contribution of climate factors (temperature/T, humidity/H, zonal wind/U, meridional
 670 wind/V) and emission (E) to changes in monthly PM_{2.5} concentration (Δ PM_{2.5}) in 2060s under G4
 671 (“mitigation”) relative to 2010s. Top figures (**a-e**) are ISIMIP results, and bottom figures (**f-j**) are
 672 WRF results. Stippling indicates the changes are insignificant at the 5% significant level in the
 673 Wilcoxon test. The grey areas represent the collinearity in the MLR, and they exist in the panel a, f

674 and h.

675

676 Next, we quantify the contribution of different meteorological factors and PM_{2.5}
677 emissions to Δ PM_{2.5} between G4 (“mitigation”) in the 2060s and the 2010s (Fig. 12).
678 Both ISIMIP and WRF results show that the increase of temperature and decrease of
679 PM_{2.5} emission play positive roles in reducing PM_{2.5} concentration. ISIMIP results (Fig.
680 12a-e), suggest that the projected increase of temperature could explain 0-20% of the
681 decrease of PM_{2.5} concentration, and decrease of PM_{2.5} emission could explain more
682 than 90% of changes in PM_{2.5} concentration differences in most of areas. Changes in
683 humidity and westerly winds (positive U-wind) do not cause significant changes in
684 Δ PM_{2.5}, but projected increases southerly wind (positive V-wind) is detrimental to the
685 decrease in PM_{2.5} concentration, and has a 0-10% negative effect on Δ PM_{2.5} in
686 Zhangjiakou. WRF results show similar spatial pattern in effect of temperature and
687 emission on Δ PM_{2.5} with ISIMIP results. Although temperature is projected to increase
688 over the whole domain (Fig. S22), there are negative contributions on Δ PM_{2.5} to the
689 north of Beijing due to increase of PM_{2.5} caused by the negative correlation between
690 PM_{2.5} and its emissions (Fig. S26). The \sim 1-2% increase of humidity leads to \sim 10%
691 increase of PM_{2.5} concentration in the south of Beijing (Fig. 12g), and 0.2-0.3 m/s
692 decreases of U-wind leads to 0-10% increase of PM_{2.5} concentration in Zhangjiakou (Fig.
693 12h). The changes in each factor in ISIMIP and WRF results are shown in Fig. S21 and
694 Fig. S22, respectively.



695

696 **Figure 13.** Contribution of climate factors (as in Fig. 12) to changes in monthly PM_{2.5} concentration
697 in 2060s under G4 with aerosol “mitigation” relative to 2060s under RCP4.5 with aerosol
698 “mitigation”. Top figures (a-e) are ISIMIP results, and bottom figures (f-j) are WRF results.
699 Stippling indicates the changes are insignificant at the 5% significant level in the Wilcoxon test. The
700 grey areas represent the collinearity in the MLR, and they exist in the panel a, f and h.

701

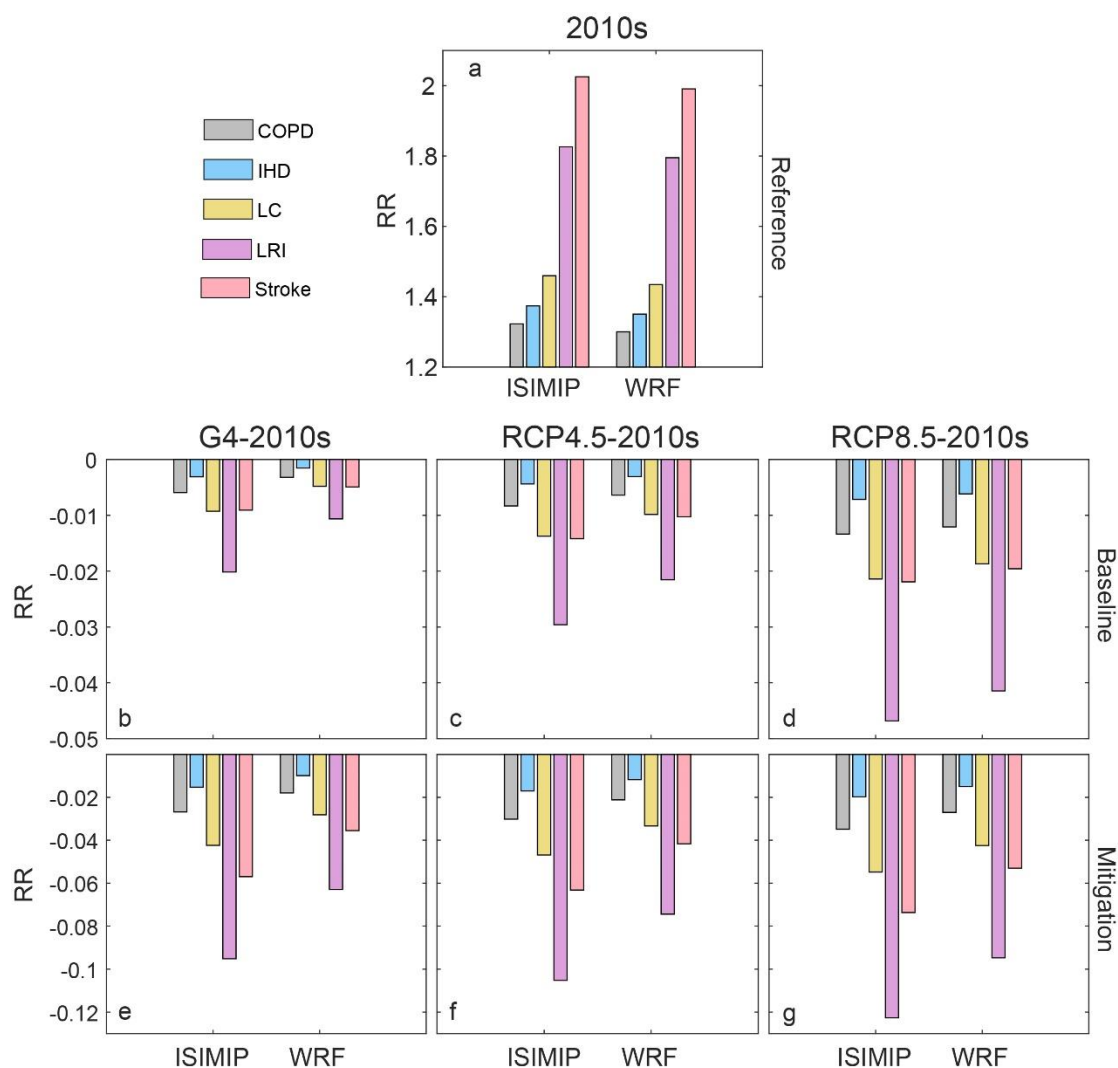
702 Now we explore the contribution of each meteorological factor to Δ PM_{2.5} between G4
703 (“mitigation”) and RCP4.5 (“mitigation”) in the 2060s (Fig. 13). The higher PM_{2.5}
704 under G4 is mainly caused by the lower temperature. In ISIMIP, lower temperature
705 explains more than 90% (100% in some places) of the raised PM_{2.5} relative to RCP4.5,

706 although the increase of humidity is also helpful to lower $PM_{2.5}$ in the western domain
707 (Fig. 13a-b). Humidity can increase suspended particle mass and coagulation,
708 promoting deposition (Li et al., 2015). The contribution of differences in U-wind and
709 V-wind on $\Delta PM_{2.5}$ is insignificant (Fig. 13c-d). In WRF, the projected lower
710 temperatures explain more than 70% of the higher $PM_{2.5}$ under G4 relative to RCP4.5
711 (Fig. 13e). Although the increase of southerly (V) wind contributes 10-20% to the
712 higher $PM_{2.5}$ in the northern domain under HadGEM2-ES and BNU-ESM (Fig. S24),
713 it is insignificant in the ensemble (Fig. 13h). Decreased westerlies (U wind) explains
714 about between +100% and -100% of $PM_{2.5}$ differences (Fig. 13g), since U-wind impacts
715 vary spatially (Fig. S26).

716

717 **3.3.3 $PM_{2.5}$ impact on health risks now and in the 2060s**

718 Changes in RR of $PM_{2.5}$ for the 5 diseases under the geoengineering and global
719 warming climate scenarios and different emission scenarios during 2060s relative to
720 2010s for the Beijing-Tianjin province are shown in Fig. 14. Present-day $PM_{2.5}$ related
721 RRs are 1.32 (1.30), 1.37 (1.35), 1.46 (1.43), 1.83 (1.80) and 2.03 (1.99) for chronic
722 obstructive pulmonary disease (COPD), ischemic heart disease (IHD), lung cancer (LC),
723 lung respiratory infection (LRI) and stroke according to the ISIMIP (WRF) simulations
724 (Fig. 14a). RR of LRI is the highest and COPD is the lowest in the five diseases, and
725 WRF estimates of RR are 0.02-0.03 lower than those of ISIMIP. In both the “baseline”
726 and “mitigation” emission scenarios, RRs will be lower under G4, RCP4.5 and RCP8.5
727 compared with the 2010s. Smaller RR reductions occur under G4 than under RCP4.5
728 and RCP8.5, and ISIMIP simulates larger reductions than WRF. This is because the
729 $PM_{2.5}$ concentrations from ISIMIP are reduced more than with WRF (Table S3). Under
730 the “baseline” emission scenario (Fig. 14b-d), the biggest reduction of RR for LRI is
731 0.047 under RCP8.5 in ISIMIP, and RRs for other diseases are projected to reduce by
732 no more than 0.02. Under the “mitigation” emission scenario (Fig. 14e-g), reductions
733 in RRs are 3-6 times greater.



734

735 **Figure 14.** Average population-weighted relative risks of PM_{2.5} related 5 diseases in 2010s (a) and
 736 its changes between G4 and 2010s (b, e), between RCP4.5 and 2010s (c, f) and between RCP8.5
 737 and 2010s (d, g) in Beijing-Tianjin province based on the ISIMIP and WRF results, respectively.
 738 PM_{2.5} concentration is based on the “baseline” emissions under G4, RCP4,5 and RCP8.5 in the
 739 middle 3 figures (b-d), and it is based on the “mitigation” emissions under G4, RCP4,5 and RCP8.5
 740 in the bottom 3 figures (e-g).

741

742 4. Discussion

743 4.1 Apparent temperature

744

745 Both ISIMIP and WRF can reproduce the observed (CN05.1) spatial patterns and
 746 seasonal variabilities of apparent temperature in the region around Beijing. WRF shows
 747 warm biases in AP during all months relative to CN05.1 due to warmer temperatures in
 748 urban areas, with the exception of BNU-ESM and HadGEM2-ES driven summers (Fig.
 749 S13). Both ISIMIP and WRF tend to overestimate population weighted NdAP₃₂ by

750 370% and 590%, respectively. These large discrepancies are due to relatively small
751 overestimates of the likelihood of the tails of the probability distributions which leads
752 to a dramatic increase in the frequency of extreme climate events (Dimri et al., 2018;
753 Huang et al., 2021). AP is about 1.5°C warmer than 2 m temperature over the Beijing
754 and Tianjin urban areas in summer due to higher vapor pressures amplifying warmer
755 urban temperatures, and this is despite humidity being lower over the cities. Under high
756 humidity conditions, a slight increase in temperature will cause a large increase in heat
757 stress (Li et al., 2018; Luo and Lau, 2019). AP is nearly 4°C colder than 2 m temperature
758 in winter due to wind speed (Fig. 2d). Differences between AP and 2 m temperature
759 (AP-T) during summer are greater in urban areas than neighboring rural areas.

760

761 The apparent temperatures in Beijing Tianjin urban areas under G4 in the 2060s are
762 simulated to be 1°C and 2.5°C lower than RCP4.5 and RCP8.5, although AP would be
763 higher than in the recent past. The cooling effect of G4 relative to RCP4.5 and RCP8.5
764 is greatest under HadGEM2-ES (Fig. S14, S15), due to the ESM having largest
765 temperature differences between scenarios (Wang et al., 2022). WRF downscaling
766 produces reduced seasonality in AP compared with ISIMIP, and WRF produces
767 relatively cooler summers and warmer winters than ISIMIP, and so much less
768 differences in apparent temperature ranges (Fig. 15). Differences in AP between G4 and
769 the RCP scenarios are mainly driven by temperature. In all scenarios and downscalings
770 AP rises faster than the temperature due to decreased wind speeds in the future (Li et
771 al., 2018; Zhu et al., 2021) but mainly because of rises in vapor pressure driven by
772 rising temperatures. This effect occurs despite the general drying expected under solar
773 geoengineering (Bala et al., 2008; Yu et al., 2015).

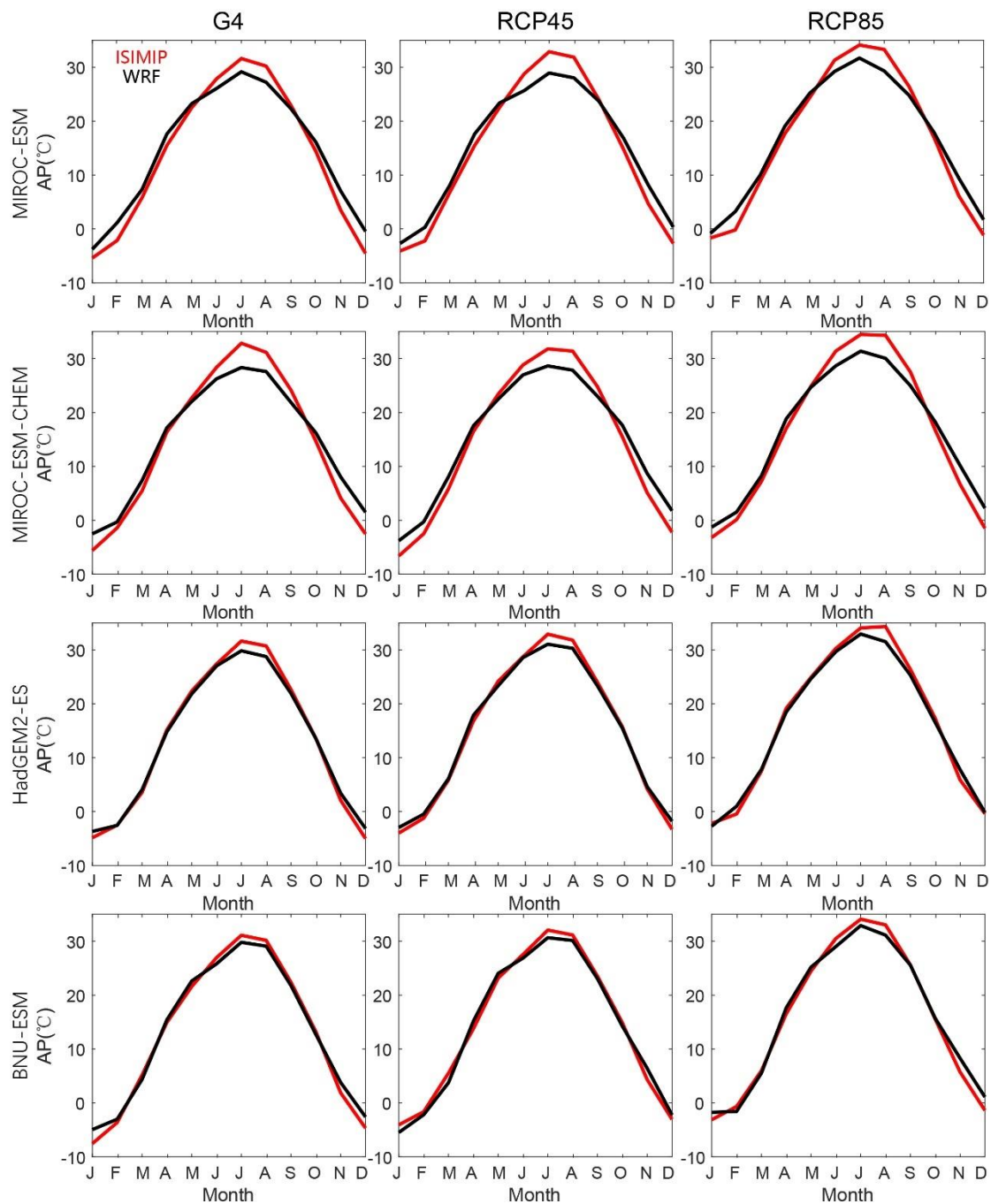
774

775 The NdAP_32 under G4 is projected to decrease by 8.6 days per year by ISIMIP and
776 6.3 days per year by WRF relative to RCP4.5 for Beijing-Tianjin Province. Much larger
777 reductions in NdAP_32 of 33.5 days per year (ISIMIP) and 19.6 days per year (WRF)
778 are projected relative to RCP8.5. Differences between scenarios in frequency of
779 dangerously hot days are far larger using ISIMIP statistical downscaling than using
780 WRF. This is another impact of the reduced seasonality of WRF compared with ISIMIP
781 (Fig. 15).

782

783 The higher resolution WRF simulation produces a much larger range of apparent
784 temperatures across the domain than CN05.1 and ISIMIP downscaling. This increased
785 variability makes reaching a statistical significance threshold more challenging for
786 WRF than ISIMIP results. Despite this, the ESM-driven differences in WRF output are
787 less than from ISIMIP, reflecting the physically based processes in the dynamic WRF
788 simulation. This reduces the impact of differences in ESM forcing at the domain
789 boundaries with WRF compared with the statistical bias correction and downscaling
790 methods. Although there are some uncertainties between models and downscaling
791 methods, G4 SAI can not only reduce the mean apparent temperature but also decrease
792 the probability of PDF tails (extreme events) in summer.

793



794

795 **Figure 15.** Seasonal cycles of apparent temperature from MIROC-ESM, MIROC-ESM-CHEM,
 796 HadGEM2-ES and BNU-ESM under G4, RCP4.5 and RCP8.5 in Beijing-Tianjin urban areas during
 797 2060s based on ISIMIP (red) and WRF (black) methods.

798

799 **4.2 PM_{2.5}**

800 We established a set spatially gridded MLR models based on the 4 ESMs downscaled
 801 variables under ISIMIP and WRF. The meteorological factors impact PM_{2.5} in complex
 802 ways, but the simple spatially gridded MLR models display enough skill to make some
 803 illustrative projections of future PM_{2.5} explaining about 70% of the variance during the
 804 historical period. PM_{2.5} concentration is correlated with emissions and anti-correlated

805 with temperature in most parts of the domain (Fig. S25-S26). Increased turbulence
806 increases diffusion of PM_{2.5} (Yang et al., 2016), and higher temperatures increase
807 evaporation losses (Liu et al., 2015) of ammonium nitrate (Chuang et al., 2017), and
808 other components (Wang et al., 2006). Humidity may have both positive and negative
809 effects on PM_{2.5} (Chen et al., 2020). It causes more water vapor to adhere to the surface
810 of PM_{2.5}, thereby increasing its mass concentration and facilitating aerosol growth
811 (Cheng et al., 2017; Liao et al., 2017). However, when the humidity exceeds a certain
812 threshold, coagulation and particle mass increases rapidly, promoting deposition (Li et
813 al., 2015). So, the slope coefficients between PM_{2.5} and humidity are positive in low
814 humidity areas, including southern plain and the Beijing-Tianjin province, but negative
815 in some northern mountain areas (Fig. S25, S26).

816

817 There are large spatial differences in wind speed and direction impacts on PM_{2.5}. Yang
818 et al. (2016) found that weaker northerly and westerly winds tend to increase the PM_{2.5}
819 concentration in northern and eastern China, respectively. The effects of wind direction
820 depend on the distribution of emitted PM_{2.5} and the condition of the underlying surface
821 (Chen et al., 2020). Most sources of PM_{2.5} lie to the south of our domain, relatively
822 clean conditions prevail to the north, so northerly winds tend to advect clean air, while
823 southerlies bring high concentrations of aerosols. Weak winds tend to increase PM_{2.5}
824 and smog formation due to sinking air and weak diffusion (Su et al., 2017; Yang et al.,
825 2017).

826

827 Xu et al. (2021) projected 2030 PM_{2.5} concentrations will decrease by 8.8% and 5.5%
828 under RCP4.5 and RCP8.5 respectively relative to 2015. Wang et al. (2021) also
829 projected decreasing trends in China under RCP4.5 and RCP8.5 during 2030-2050.
830 There were seasonal changes in PM_{2.5} concentration differences between RCP4.5/8.5
831 scenarios and the historical scenario near the Bohai Sea (Dou et al., 2021). However,
832 there are also some simulations where PM_{2.5} concentrations increase in warmer climates.
833 Hong et al. (2019) suggest that annual mean PM_{2.5} concentrations will increase 1-8
834 $\mu\text{g}/\text{m}^3$ in an area including Beijing and Tianjin under RCP4.5 during 2046-2050,
835 compared with 2006-2010. These inconsistent responses are mainly caused by the
836 differences in the selection of ESMs, chemical transport models and climate/emission
837 scenarios. Different RCP scenarios not only correspond to different future climate states,
838 but also have different anthropogenic emissions of air pollutants. In our study, we do
839 not consider the PM_{2.5} emission differences between RCP4.5 and RCP8.5, and instead
840 applied the ECLIPSE PM_{2.5} emission scenarios in our MLR projection.

841

842 Emissions reductions are expected to play the dominant role in the decrease of PM_{2.5}
843 concentrations under G4 aerosol “mitigation” in 2060s (Fig. 12). Meteorological
844 changes under the different future scenarios make much smaller changes as evidenced
845 by the scenarios using “baseline” – that is present day PM_{2.5} emissions, with decreases
846 in mean annual concentration of 1.0 (1.3), 1.8 (2.0), 3.3 (3.2) $\mu\text{g}/\text{m}^3$ over Beijing-

847 Tianjin province under G4, RCP4.5 and RCP8.5 with WRF (ISIMIP), (Table S3), which
848 are mainly caused by the temperature increases (Fig. 13). The negative relationships
849 between emission and PM_{2.5} concentration result in the increase of PM_{2.5} under G4
850 (“mitigation”) relative to 2010s in the north of Beijing with WRF. This may be due to
851 changes in PM_{2.5} out of the domain being opposite to those in domain during the MLR
852 fitting period, since relocation of polluting sources from the urban areas mainly to the
853 west, was occurring over the calibration period. The accuracy of PM_{2.5} emission data is
854 also crucial for training MLR models, and PM_{2.5} data was sparse before 2013, relying
855 on reconstructions based on satellite optical depth estimates. Although both increase of
856 temperature and decrease of emission explain more than 90% of the decrease in PM_{2.5}
857 in most areas, there are large spatial differences due to wind and humidity. On the one
858 hand, there is uncertainty in the differences in changes of wind speed and humidity
859 between different ESMs and downscaling methods; on the other hand, the complex
860 physical relationship between them and PM_{2.5} also increases uncertainties. Reductions
861 in PM_{2.5} in the future are projected to decrease PM_{2.5} related health issues, although its
862 effect on different diseases are different. Changes in PM_{2.5} related risk between G4 and
863 RCPs are from 1-3%, with PM_{2.5} emissions policy dominating differences over climate
864 scenario.

865

866 There are some differences in projecting PM_{2.5} concentration between WRF and ISIMIP
867 methods. Compared to the 2010s reference, PM_{2.5} concentration in ISIMIP are
868 projected to decrease more than using WRF in G4 under the “mitigation” scenario
869 during the 2060s over the Tianjin province (Fig. 11a, e). However, the spatial patterns
870 of changes in PM_{2.5} concentration between G4 and RCP4.5/8.5 under the “mitigation”
871 scenario during 2060s are similar (Fig. 11c-d, g-h). This means that the effects of
872 different downscaled methods on projecting PM_{2.5} are small if we only consider the
873 climate change alone without considering emissions changes. Due to the larger
874 regression coefficient of emissions in the MLR under the ISIMIP method (Fig. S25,
875 S26), the negative changes in PM_{2.5} concentration are larger between “mitigation” and
876 baseline under G4 during 2060s than that under the WRF method. Correspondingly, the
877 ISIMIP method has a greater reduction in PM_{2.5} related RR than WRF under three future
878 climate scenarios during the 2060s.

879

880 Eastham et al. (2018) deduced from experiments using 1 Tg/yr SAI in a coupled
881 chemistry-transport model directly simulating atmospheric chemistry, transport,
882 radiative transfer of UV, emissions, and loss processes, that per unit mass emitted,
883 surface-level emissions of sulfate result in 25 times greater population exposure to
884 PM_{2.5} than emitting the same aerosol into the stratosphere. The G4 experiment specifies
885 5 Tg/yr injection rate, which over our domain would equate to 1450 t/yr if it was
886 deposited uniformly globally (which it certainly would not be). Reducing this by the
887 1/25 factor amounts to 58 t/yr which can be compared with present PM_{2.5} emissions of
888 around 3.3×10^5 t/year in our domain. If we consider the aerosol deposition under G4
889 scenarios, PM_{2.5} concentration will be 0-1 $\mu\text{g}/\text{m}^3$ higher than that without due to

890 deposition of the SAI aerosols (Fig. S27), and RR is projected to increase by 0.01% for
891 Beijing-Tianjin province (Table S4). This comparison suggests that tropospheric
892 emissions will be much more important for human health in our domain than from the
893 SAI specified by G4.

894

895 The most important change in $PM_{2.5}$ will come from emissions reductions, with the
896 different weather conditions under both G4 and RCP scenarios making relatively little
897 practical differences in concentrations. $PM_{2.5}$ concentration is expected to decrease
898 significantly (ISIMIP: $-7.6\mu g/m^3$, WRF: $-5.4\mu g/m^3$) in the Beijing-Tianjin province,
899 but they will still not meet either Chinese or international standards. The temperature
900 under G4 is lower than that under RCP4.5 and RCP8.5 scenarios, which makes the
901 $PM_{2.5}$ concentration under G4 higher. But the difference in $PM_{2.5}$ between the two is
902 small and even within uncertainty due to projected differences in humidity and wind.
903 Potentially improved estimates from more complex models such as WRF-Chem,
904 CMAQ and GEOS-Chem over the simple MLR methods used here will be of limited
905 value unless the differences between the ESM driving these models is reduced. It can
906 be confirmed that emission policies based on the 13th Five Year Plan are not enough,
907 and higher emission standards need to be developed for a healthy living environment.

908

909 Our study did not consider the impacts of socio-economic pathways on $PM_{2.5}$ future
910 emissions, instead we explore the meteorological differences between the SAI G4
911 scenario and the greenhouse gas RCP4.5/RCP8.5 on $PM_{2.5}$ concentrations. $PM_{2.5}$
912 emissions were defined by the uncontrolled (“baseline”) and a scenario where
913 technological intervention (“mitigation”) reduces emissions. There are some limitations
914 in our study. Firstly, the HTAP_V3 dataset only includes anthropogenic $PM_{2.5}$ emission,
915 not natural $PM_{2.5}$ emission. Natural $PM_{2.5}$ will also change in the future under changing
916 climate. The sources of natural $PM_{2.5}$ include the sandstorms that sometimes occur in
917 spring as extreme winds mobilize dry unvegetated soils. These relatively extreme
918 conditions are difficult to simulate in ESM and subject to land use policy e.g., the
919 numerous ecosystem service measures undertaken by China over the last five decades
920 (Miao et al.,2015). Secondly, although $PM_{2.5}$ concentration includes both primary and
921 secondary $PM_{2.5}$ during model training, we do not consider the precursor gases for
922 secondary $PM_{2.5}$ directly. The sensitivity of MLR may diminish at the high $PM_{2.5}$ values
923 when secondary $PM_{2.5}$ dominates the variability of total $PM_{2.5}$ (Upadhyay et al., 2018).
924 Thirdly, we only consider the effect of dominant near-surface meteorological variables
925 on the $PM_{2.5}$. However, the vertical transport of pollutants related to vertical
926 atmospheric stability should not be ignored (Lo et al., 2006; Wu et al., 2005), and this
927 may contribute to the differences in RCP4.5 scenario from our MLR model and more
928 sophisticated simulations (Fig. S7). Finally, although it is insignificant for the Beijing
929 and Tianjin provinces, the MLR model suffers collinearity problems in some areas.
930 These factors play smaller roles as we are mainly considering changes in $PM_{2.5}$
931 concentration between different climate scenarios. Nevertheless, projection for changes

932 in PM_{2.5} between SAI scenarios and per greenhouse gas scenarios would be valuable
933 for global air quality impacts from geoengineering.

934

935 **5. Conclusion**

936 Our study on thermal comfort and aerosol pollution under geoengineering scenarios for
937 the Beijing megalopolis may be useful across the developing world, which is expected
938 to suffer disproportionate climate impact damages relative the global mean, while also
939 undergoing rapid urbanization. Assessing health impacts and mortality due to heat
940 stress and PM_{2.5} under greenhouse gas scenarios should consider urbanization and the
941 change to concrete surfaces from vegetation that leads to differences in heat capacities,
942 rates of evapotranspiration, and hence humidity and apparent temperature. These
943 require downscaled analyses, accurate meteorological and high-resolution land surface
944 datasets, and industrial development scenarios.

945

946 In our analysis we assumed the urban area did not change over time, and also that
947 population remains distributed as in the recent past. This may be reasonable in the
948 highly developed and relatively mature greater Beijing-Tianjin region but should be
949 considered in rapidly urbanizing regions elsewhere. There certainly will be changes
950 over time in the radiative cooling from surface pollution sources. PM_{2.5} is a health issue
951 in many developing regions (Ran et al., 2023), but as wealth increases efforts to curb
952 air pollution generally clean the air. This has clear health benefits, but also removes
953 aerosols from the troposphere that cool the surface. The urban areas that have higher
954 apparent temperatures at present are also the areas with greatest aerosol load and hence
955 greatest cooling. Once that is removed direct radiation, air temperatures and apparent
956 temperatures will all rise – by several degrees (Wang et al., 2016). So, a future more
957 comprehensive health impact study would include both the negative health impacts of
958 aerosol pollution and the potential cooling effects those aerosols produce. Additionally,
959 the formulation of apparent temperature used does not consider the effect of radiation
960 on human comfort (Kong and Huber, 2022). When PM_{2.5} levels are high there is no
961 shade because the sky is milky-white, similarly SAI will brighten the sky (Kravitz et
962 al., 2012). Comfort is increased in clear sky conditions when shade is readily found.

963

964 The changes simulated to relative risk from increased PM_{2.5} under the G4 SAI scenario
965 are about 1-3% worse than under RCP4.5, mainly because of lower temperatures under
966 G4. The difference this would make to the overall health burden under SAI depends on
967 the range of other impacts that include changes in apparent temperature we discuss. G4
968 reduces the number of days with AP>32 (when extreme caution is advised) by 6-8 per
969 year relative to RCP4.5 and by 20-34 relative to RCP8.5. But G4 itself will still increase
970 these extreme caution days by 1-20 relative to conditions in the 2010s. Lowering PM_{2.5}
971 emissions will increase ground temperatures and the associated risk of dangerous
972 apparent temperatures will also increase rapidly as the distribution of temperatures is
973 shifted making presently rare hot events into much more frequent heat waves.

974 **Code and data availability**

975 All ESM data used in this work are available from the Earth System Grid Federation
976 (WCRP, 2021; <https://esgf-node.llnl.gov/projects/cmip6>, last access: 14 July 2021).
977 The WRF and ISIMIP bias-corrected and downscaled results are available for the
978 authors on request. WRF and ISIMIP codes are freely available at the references cited
979 in the methods sections.

980 **Supplement link**

981 The link to the supplement will be included by Copernicus.

982 **Author contribution**

983 JCM and LZ designed the experiments, JW performed the simulations. All the authors
984 wrote the manuscript.

985 **Competing interests**

986 The authors declare that they have no conflict of interest.

987 **Disclaimer**

988 Publisher's note: Copernicus Publications remains neutral with regard to jurisdictional
989 claims in published maps and institutional affiliations.

990 **Special issue statement:**

991 This article is part of the special issue "Resolving uncertainties in solar geoengineering
992 through multi-model and large-ensemble simulations (ACP/ESD inter-journal SI)". It
993 is not associated with a conference.

994 **Acknowledgements**

995 We thank the editor and two constrictive referees for improving the manuscript. This
996 work relies on the climate modeling groups participating in the Geoengineering Model
997 Intercomparison Project and their model development teams; the CLIVAR/WCRP
998 Working Group on Coupled Modeling for endorsing the GeoMIP; and the scientists
999 managing the earth system grid data nodes who have assisted with making GeoMIP
1000 output available. This research was funded by the National Key Science Program for
1001 Global Change Research (2015CB953602).

1002

1003 **References**

- 1004 Burnett, R., Pope III, C., Ezzati, M., Olives, C., Lim, S., Mehta, S., Shin, H., Singh, G.,
1005 Hubbell, B., Brauer, M., Anderson, A., Smith, K., Balmes, J., Bruce, N., Kan, H.,
1006 Laden, F., Prüss-Ustün, A., Turner, M., Gapstur, S., Diver, W., and Cohen, A.: An
1007 Integrated Risk Function for Estimating the Global Burden of Disease Attributable
1008 to Ambient Fine Particulate Matter Exposure, *Environ., Health Perspect.*, 122, 397-
1009 403, <https://doi.org/10.1289/ehp.1307049>, 2014.
- 1010 Bala, G., Duffy, P. B., Taylor, K. E.: Impact of geoengineering schemes on the global
1011 hydrological cycle, *Proc. Natl. Acad. Sci. USA*, 105 (22), 7664-7669,
1012 <https://doi.org/10.1073/pnas.0711648105>, 2008.
- 1013 Chen, Z., Cai, J., Gao, B., Xu, B., Dai, S., He, B., Xie, X.: Detecting the causality
1014 influence of individual meteorological factors on local PM_{2.5} concentrations in the
1015 Jing-Jin-Ji region, *Sci. Rep.*, 7, 40735, <https://doi.org/10.1038/srep40735>, 2017.
- 1016 Chen, Z., Chen, D., Kwan, M.-P., Chen, B., Gao, B., Zhuang, Y., Li, R., and Xu, B.: The
1017 control of anthropogenic emissions contributed to 80 % of the decrease in
1018 PM_{2.5} concentrations in Beijing from 2013 to 2017, *Atmos. Chem. Phys.*, 19, 13519–
1019 13533, <https://doi.org/10.5194/acp-19-13519-2019>, 2019.
- 1020 Chen, Z., Chen, D., Zhao, C., Kwan, M., Cai, J., Zhuang, Y., Zhao, B., Wang, X., Chen,
1021 B., Yang, J., Li, R., He, B., Gao, B., Wang, K., and Xu, B.: Influence of
1022 meteorological conditions on PM_{2.5} concentrations across China: A review of
1023 methodology and mechanism, *Environ. Int.*, 139, 105558,
1024 <https://doi.org/10.1016/j.envint.2020.105558>, 2020.
- 1025 Chen, Z., Xie, X., Cai, J., Chen, D., Gao, B., He, B., Cheng, N., and Xu, B.:
1026 Understanding meteorological influences on PM_{2.5} concentrations across China: a
1027 temporal and spatial perspective, *Atmos. Chem. Phys.*, 18, 5343–5358,
1028 <https://doi.org/10.5194/acp-18-5343-2018>, 2018.
- 1029 Cheng, L., Meng, F., Chen, L., Jiang, T., and Su, L.: Effects on the haze pollution from
1030 autumn crop residue burning over the Jing-Jin-Ji Region, *China Environ. Sci.*, 37,
1031 2801–2812, 2017.
- 1032 Chi, X., Li, R., Cubasch, U., Cao, W.: The thermal comfort and its changes in the 31
1033 provincial capital cities of mainland China in the past 30 years, *Theor. Appl.*
1034 *Climatol.*, 132(1-2), 599–619, 2018.
- 1035 Chuang, M., Chou, C., Lin, N., Takami, A., Hsiao, T., Lin, T., Fu, J., Pani, S., Lu, Y., and
1036 Yang, T.: A simulation study on PM_{2.5} sources and meteorological characteristics at
1037 the northern tip of Taiwan in the early stage of the Asian haze period, *Aerosol Air*
1038 *Qual. Res.*, 17, 3166-3178, <https://doi.org/10.4209/aaqr.2017.05.0185>, 2017.
- 1039 Collins, W. J., Bellouin, N., Doutriaux-Boucher, M., Gedney, N., Halloran, P., Hinton,
1040 T., Hughes, J., Jones, C. D., Joshi, M., Liddicoat, S., Martin, G., O’Connor, F., Rae,
1041 J., Senior, C., Sitch, S., Totterdell, I., Wiltshire, A., Woodward, S.: Development
1042 and evaluation of an Earth-System model – HadGEM2, *Geosci. Model Dev.*, 4,
1043 1051–1075, <https://doi.org/10.5194/gmd-4-1051-2011>, 2011.
- 1044 Curry, C. L., Sillmann, J., Bronaugh, D., Alterskjaer, K., Cole, J. N. S., Ji, D., Kravitz,
1045 B., Kristjánsson, J. E., Moore, J. C., Muri, H., Niemeier, U., Robock, A., Tilmes, S.,

1046 and Yang, S.: A multimodel examination of climate extremes in an idealized
1047 geoengineering experiment, *J. Geophys. Res.-Atmos.*, 119, 3900–3923,
1048 <https://doi.org/10.1002/2013JD020648>, 2014.

1049 Dimri, A. P., Kumar, D., Choudhary, A., Maharana, P.: Future changes over the
1050 Himalayas: Maximum and minimum temperature, *Global and Planetary Change*,
1051 162, 212–234, <https://doi.org/10.1016/j.gloplacha.2018.01.015>, 2018.

1052 Dou, C., Ji, Z., Xiao, Y., Zhu, X., and Dong, W.: Projections of air pollution in northern
1053 China in the two RCPs scenarios, *Remote Sens.*, 13, 3064,
1054 <https://doi.org/10.3390/rs13163064>, 2021.

1055 Eastham, D., Weisenstein, D., Keith, D., and Barrett, A.: Quantifying the impact of
1056 sulfate geoengineering on mortality from air quality and UV-B exposure, *Atmos.*
1057 *Environ.*, 187, 424–434. DOI: <http://dx.doi.org/10.1016/j.atmosenv.2018.05.047>,
1058 2018.

1059 Fan, M., Zhang, Y., Lin, Y., Cao, F., Sun, Y., Qiu, Y., Xing, G., Dao, X., and Fu, P.:
1060 Specific sources of health risks induced by metallic elements in PM_{2.5} during the
1061 wintertime in Beijing, China, *Atmos. Environ.*, 246, 118112,
1062 <https://doi.org/10.1016/j.atmosenv.2020.118112>, 2021.

1063 Fischer, E., and Knutti, R.: Robust projections of combined humidity and temperature
1064 extremes, *Nat. Clim. Change*, 3, 126–130, <https://doi.org/10.1038/nclimate1682>,
1065 2013.

1066 Foley, K. M., Roselle, S. J., Appel, K. W., Bhave, P. V., Pleim, J. E., Otte, T. L., Mathur,
1067 R., Sarwar, G., Young, J. O., Gilliam, R. C., Nolte, C. G., Kelly, J. T., Gilliland, A.
1068 B., and Bash, J. O.: Incremental testing of the Community Multiscale Air Quality
1069 (CMAQ) modeling system version 4.7, *Geosci. Model Dev.*, 3, 205–226,
1070 <https://doi.org/10.5194/gmd-3-205-2010>, 2010.

1071 Fu, J., Jiang, D., Huang, Y.: 1 km Grid Population Dataset of China, *Digital Journal of*
1072 *Global Change Data Repository*, <https://doi.org/10.3974/geodb.2014.01.06.V1>,
1073 2014.

1074 Garcia, F. C., Bestion, E., Warfield, R., Yvon-Durocher, G.: Changes in temperature alter
1075 the relationship between biodiversity and ecosystem functioning, *Proc. Natl. Acad.*
1076 *Sci. U.S.A.*, 115, 10989–10999, <https://doi.org/10.1073/pnas.1805518115>, 2018.

1077 Grinsted, A., Moore, J., and Jevrejeva, S.: Projected Atlantic tropical cyclone threat from
1078 rising temperatures, *PNAS*, 110, 5369–5373, <https://doi/10.1073/pnas.1209980110>,
1079 2013.

1080 Grundstein, A. and Dowd, J.: Trends in extreme apparent temperatures over the United
1081 States, 1949–2010, *J. Appl. Meteorol. Climatol.*, 50(8), 1650–1653,
1082 <https://doi.org/10.1175/JAMC-D-11-063.1>, 2011.

1083 Guan, W., Zheng, X., Chung, K., and Zhong, N.: Impact of air pollution on the burden
1084 of chronic respiratory diseases in China: time for urgent action, *Lancet*, 388, 1939–
1085 1951, [https://doi.org/10.1016/S0140-6736\(16\)31597-5](https://doi.org/10.1016/S0140-6736(16)31597-5), 2016.

1086 Guo, L., Zhang, Y., Lin, H., Zeng, W., Liu, T., Xiao, J., Rutherford, S., You, J., Ma, W.:
1087 The washout effects of rainfall on atmospheric particulate pollution in two Chinese
1088 cities, *Environ. Pollut.*, 215, 195–202, <https://doi.org/10.1016/j.envpol.2016.05.003>,
1089 2016.

- 1090 Han, J., Wang, J., Zhao, Y., Wang, Q., Zhang, B., Li, H., and Zhai, J.: Spatio-temporal
1091 variation of potential evapotranspiration and climatic drivers in the Jing-Jin-Ji region,
1092 North China, *Agric. For. Meteorol.*, 256, 75-83,
1093 <https://doi.org/10.1016/j.agrformet.2018.03.002>, 2018.
- 1094 Hempel, S., Frieler, K., Warszawski, L., Schewe, J., and Piontek, F.: A trend-preserving
1095 bias correction – the ISI-MIP approach, *Earth Syst. Dynam.*, 4, 219–236,
1096 <https://doi.org/10.5194/esd-4-219-2013>, 2013.
- 1097 Hersbach, H., Bell, B., Berrisford, P., Biavati, G., Horányi, A., Muñoz Sabater, J.,
1098 Nicolas, J., Peubey, C., Radu, R., Rozum, I., Schepers, D., Simmons, A., Soci, C.,
1099 Dee, D., Thépaut, J-N.: ERA5 hourly data on pressure levels from 1979 to present,
1100 Copernicus Climate Change Service (C3S) Climate Data Store (CDS),
1101 <https://doi.org/10.24381/cds.bd0915c6>, 2018.
- 1102 Ho, H. C., Knudby, A., Xu, Y., Hodul, M., Aminipouri, M.: A comparison of urban heat
1103 islands mapped using skin temperature, air temperature, and apparent temperature
1104 (Humidex), for the greater Vancouver area, *Science of The Total Environment*, 544,
1105 929-938, <https://doi.org/10.1016/j.scitotenv.2015.12.021>, 2016.
- 1106 Hong, C., Zhang, Q., Zhang, Y., Davis, S., Tong, D., Zheng, Y., Liu, Z., Guan, D., He,
1107 K., and Schellnhuber, H. J.: Impacts of climate change on future air quality and
1108 human health in China, *PNAS*, 116, 17193-17200,
1109 <https://doi.org/10.1073/pnas.1812881116>, 2019.
- 1110 Huang, J., Li, Q., Song, Z.: Historical global land surface air apparent temperature and
1111 its future changes based on CMIP6 projections, *Science of The Total Environment*,
1112 816, 151656, <https://doi.org/10.1016/j.scitotenv.2021.151656>, 2021.
- 1113 IPCC, 2021. Climate change 2021: the physical science basis. In: Masson-Delmotte, V.,
1114 Zhai, P., Pirani, A., Connors, S.L., Péan, C., Berger, S., Caud, N., Chen, Y., Goldfarb,
1115 L., Gomis, M.I., Huang, M., Leitzell, K., Lonnoy, E., Matthews, J.B.R., Maycock,
1116 T.K., Waterfiel, T., Yelekçi, O., Yu, R., B.Z. (Eds.), *Contribution of Working
1117 Group I to the Sixth Assessment Report of the Intergovernmental Panel on Climate
1118 Change*. Cambridge University Press In Press.
- 1119 Jacobs, S. J., Pezza, A. B., Barras, V., Bye, J., Vihma, T.: An analysis of the
1120 meteorological variables leading to apparent temperature in Australia: present
1121 climate, trends, and global warming simulations, *Glob. Planet. Chang.*, 107, 145–
1122 156, 2013.
- 1123 Janssens-Maenhout, G., Crippa, M., Guizzardi, D., Dentener, F., Muntean, M., Pouliot,
1124 G., Keating, T., Zhang, Q., Kurokawa, J., Wankmüller, R., Denier van der Gon, H.,
1125 Kuenen, J. J. P., Klimont, Z., Frost, G., Darras, S., Koffi, B., and Li, M.: HTAP_v2.2:
1126 a mosaic of regional and global emission grid maps for 2008 and 2010 to study
1127 hemispheric transport of air pollution, *Atmos. Chem. Phys.*, 15, 11411-11432,
1128 <https://doi.org/10.5194/acp-15-11411-2015>, 2015.
- 1129 Ji, D., Fang, S., Curry, C. L., Kashimura, H., Watanabe, S., Cole, J. N. S., Lenton, A.,
1130 Muri, H., Kravita, B., Moore, J. C.: Extreme temperature and precipitation response
1131 to solar dimming and stratospheric aerosol geoengineering, *Atmospheric Chemistry
1132 and Physics*, 18, 10133-10156, <https://doi.org/10.5194/acp-18-10133-2018>, 2018.
- 1133 Ji, D., Wang, L., Feng, J., Wu, Q., Cheng, H., Zhang, Q., Yang, J., Dong, W., Dai, Y.,

1134 Gong, D., Zhang, R.-H., Wang, X., Liu, J., Moore, J. C., Chen, D., and Zhou, M.:
 1135 Description and basic evaluation of Beijing Normal University Earth System Model
 1136 (BNU-ESM) version 1, *Geosci. Model Dev.*, 7, 2039–2064,
 1137 <https://doi.org/10.5194/gmd-7-2039-2014>, 2014.

1138 Jin, H., Chen, X., Zhong, R., and Liu, M.: Influence and prediction of PM_{2.5} through
 1139 multiple environmental variables in China, *Sci. Total Environ.*, 849, 157910,
 1140 <https://doi.org/10.1016/j.scitotenv.2022.157910>, 2022.

1141 Jones, A. C., Hawcroft, M. K., Haywood, J. M., Jones, A., Guo, X., Moore, J.C.:
 1142 Regional climate impacts of stabilizing global warming at 1.5 K using solar
 1143 geoengineering, *Earth's Future*, 6, <https://doi.org/10.1002/2017EF000720>, 2018.

1144 Kim, D. H., Shin, H. J., Chung, I. U.: Geoengineering: Impact of marine cloud
 1145 brightening control on the extreme temperature change over East Asia, *Atmosphere*,
 1146 11(12), 1345, <https://doi.org/10.3390/atmos11121345>, 2020.

1147 Klimont, Z., Kupiainen, K., Heyes, C., Purohit, P., Cofala, J., Rafaj, P., Borken-Kleefeld,
 1148 J., and Schöpp, W.: Global anthropogenic emissions of particulate matter including
 1149 black carbon, *Atmos. Chem. Phys.*, 17, 8681–8723, [https://doi.org/10.5194/acp-17-](https://doi.org/10.5194/acp-17-8681-2017)
 1150 [8681-2017](https://doi.org/10.5194/acp-17-8681-2017), 2017. Kong, Q., and Huber, M.: Explicit calculations of wet-bulb globe
 1151 temperature compared with approximations and why it matters for labor productivity,
 1152 *Earth's Future*, 10, e2021EF002334, <https://doi.org/10.1029/2021EF002334>,
 1153 2022. Kraaijenbrink, P. D. A., Bierkens, M. F. P., Lutz A. F., Immerzeel, W. W.:
 1154 Impact of a global temperature rise of 1.5 degrees Celsius on Asia's glaciers, *Nature*,
 1155 549, 257-260, <https://doi.org/10.1038/nature23878>, 2017.

1156 Kravitz, B., MacMartin, D., and Caldeira, K.: Geoengineering: Whiter skies?, *Geophys.*
 1157 *Res. Lett.*, 39, L11801, <https://doi.org/10.1029/2012GL051652>, 2012.

1158 Kravitz, B., Robock, A., Boucher, O., Schmidt, H., Taylor, K. E., Stenchikov, G., and
 1159 Schulz, M.: The geoengineering model intercomparison project (GeoMIP), *Atmos.*
 1160 *Sci. Lett.*, 12(2), 162-167, <https://doi.org/10.1002/asl.316>, 2011.

1161 Kuswanto, H., Kravitz, B., Miftahurrohmah, B., Fauzi, F., Sopahaluwaken, A., and
 1162 Moore, J. C.: Impact of solar geoengineering on temperatures over the Indonesian
 1163 Maritime Continent, *Int. J. Climatol.*, 1-20, <https://doi.org/10.1002/joc.7391>, 2021.

1164 Lee, C. and Sheridan, S.: A new approach to modeling temperature-related mortality:
 1165 non-linear autoregressive models with exogenous input, *Environ. Res.*, 164:53–64,
 1166 <https://doi.org/10.1016/j.envres.2018.02.020>, 2018.

1167 Lenton, T. and Vaughan, N.: The radiative forcing potential of different climate
 1168 geoengineering options, *Atmos. Chem. Phys.*, 9, 5539–5561,
 1169 <https://doi.org/10.5194/acp-9-5539-2009>, 2009.

1170 Li, D., Wu, Q., Feng, J., Wang, Y., Wang, L., Xu, Q., Sun, Y., Cao, K., and Cheng, H.:
 1171 The influence of anthropogenic emissions on air quality in Beijing-Tianjin-Hebei of
 1172 China around 2050 under the future climate scenario, *J. Cleaner Prod.*, 388, 135927,
 1173 <https://doi.org/10.1016/j.jclepro.2023.135927>, 2023.

1174 Li, J., Chen, H., Li, Z., Wang, P., Cribb, M., and Fan, X.: Low-level temperature
 1175 inversions and their effect on aerosol condensation nuclei concentrations under
 1176 different large-scale synoptic circulations, *Adv. Atmos. Sci.*, 32, 898-908,
 1177 <https://doi.org/10.1007/s00376-014-4150-z>, 2015.

1178 Li, J., Chen, Y., Gan, T., Lau, N.: Elevated increases in human-perceived temperature
1179 under climate warming, *Nat. Clim. Chang.*, 8 (1), 43–47,
1180 <https://doi.org/10.1038/s41558-017-0036-2>, 2018.

1181 Li, K., Liao, H., Zhu, J., and Moch, J.: Implications of RCP emissions on future PM_{2.5}
1182 air quality and direct radiative forcing over China, *J. Geophys. Res. Atmos.*, 121, 12,
1183 985–13, 008, <https://doi.org/10.1002/2016JD025623>, 2016.

1184 Li, M., Klimont, Z., Zhang, Q., Martin, R. V., Zheng, B., Heyes, C., Cofala, J., Zhang,
1185 Y., and He, K.: Comparison and evaluation of anthropogenic emissions of SO₂ and
1186 NO_x over China, *Atmos. Chem. Phys.*, 18, 3433–3456, <https://doi.org/10.5194/acp-18-3433-2018>, 2018.

1188 Liao, T., Wang, S., Ai, J., Gui, K., Duan, B., Zhao, Q., Zhang, X., Jiang, W., and Sun, Y.:
1189 Heavy pollution episodes, transport pathways and potential sources of PM_{2.5} during
1190 the winter of 2013 in Chengdu (China), *Sci. Total Environ.*, 584–585, 1056–1065,
1191 <https://doi.org/10.1016/j.scitotenv.2017.01.160>, 2017.

1192 Lin, G., Fu, J., Jiang, D., Wang, J., Wang, Q., and Dong, D.: Spatial variation of the
1193 relationship between PM_{2.5} concentrations and meteorological parameters in China,
1194 *BioMed Res. Int.*, 2015, 684618, <https://doi.org/10.1155/2015/684618>, 2015.

1195 Lo, J., Lau, A., Fung, J., and Chen, F.: Investigation of enhanced cross-city transport and
1196 trapping of air pollutants by coastal and urban land-sea breeze circulations, *J.*
1197 *Geophys. Res.-Atmos.*, 111(D14), <https://doi.org/10.1029/2005JD006837>, 2006.

1198 Luo, M., & Lau, N.-C.: Characteristics of summer heat stress in China during 1979–2014:
1199 Climatology and long-term trends, *Climate Dynamics*, 53(9), 5375–5388,
1200 <https://doi.org/10.1007/s00382-019-04871-5>, 2019.

1201 Luo, M. and Lau, N.: Increasing Human-Perceived Heat Stress Risks Exacerbated by
1202 Urbanization in China: A Comparative Study Based on Multiple Metrics, *Earth’s*
1203 *Future*, 9 (7), <https://doi.org/10.1029/2020EF001848>, 2021.

1204 Lyon, B. and Barnston, A.: Diverse characteristics of US summer heat waves, *J. Clim.*,
1205 30 (19), 7827–7845, <https://doi.org/10.1175/JCLI-D-17-0098.1>, 2017.

1206 Maji, K., Ye, W., Arora, M., and Nagendra, S.: PM_{2.5}-related health and economic loss
1207 assessment for 338 Chinese cities, *Environ. Int.*, 121, 392–403,
1208 <https://doi.org/10.1016/j.envint.2018.09.024>, 2018.

1209 Matthews, T., Wilby, R., and Murphy, C.: Communicating the deadly consequences of
1210 global warming for human heat stress, *PNAS*, 114, 3861–3866,
1211 <https://doi.org/10.1073/pnas.1617526114>, 2017.

1212 Miao, L., Moore, J. C., Zeng, F., Lei, J., Ding, J., He, B., and Cui, X.: Footprint of
1213 research in desertification management in China, *Land Degrad. Dev.*, 26, 450–457,
1214 <https://doi.org/10.1002/ldr.2399>, 2015.

1215 Mishra, D., Goyal, P., and Upadhyay, A.: Artificial intelligence based approach to
1216 forecast PM_{2.5} during haze episodes: a case study of Delhi, India, *Atmos. Environ.*,
1217 102, 239–248, <https://doi.org/10.1016/j.atmosenv.2014.11.050>, 2015.

1218 Murray, F.: On the computation of saturation vapor pressure, Rand Corp Santa Monica
1219 Calif, 1966.

1220 Nguyen, G., Shimadera, H., Uranishi, K., Matsuo, T., and Kondo, A.: Numerical
1221 assessment of PM_{2.5} and O₃ air quality in Continental Southeast Asia: Impacts of

1222 future projected anthropogenic emission change and its impacts in combination with
1223 potential future climate change impacts, *Atmos. Environ.*, 226, 117398,
1224 <https://doi.org/10.1016/j.atmosenv.2020.117398>, 2020.

1225 Perkins, S. and Alexander, L.: On the measurement of heat waves, *J Clim.*, 26 (13),
1226 4500–4517, <https://doi.org/10.1175/JCLI-D-12-00383.1>, 2013.

1227 Ran, Q., Lee, S., Zheng, D., Chen, H., Yang, S., Moore, J., Dong, W.: Potential Health
1228 and Economic Impacts of Shifting Manufacturing from China to Indonesia or India,
1229 *Science of the total environment*, 855, 158634,
1230 <http://dx.doi.org/10.1016/j.scitotenv.2022.158634>, 2022.

1231 Riahi, K., Rao, S., Krey, V., Cho, C., Chirkov, V., Fischer, G., Kindermann, G.,
1232 Nakicenovic, N., Rafaj, P.: RCP 8.5—A scenario of comparatively high greenhouse
1233 gas emissions, *Climatic Change* 109, 33, [https://doi.org/10.1007/s10584-011-0149-](https://doi.org/10.1007/s10584-011-0149-y)
1234 [y](https://doi.org/10.1007/s10584-011-0149-y), 2011.

1235 Robock, A., Marquardt, A., Kravitz, B. and Stenchikov, G.: Benefits, risks, and costs of
1236 stratospheric geoengineering, *Geophys. Res. Lett.*, 36(19),
1237 <https://doi.org/10.1029/2009GL039209>, 2009.

1238 Shepherd, J.: *Geoengineering the climate: Science, governance, and uncertainty*, Royal
1239 Society Policy document 10/09, 82 pp, 2009.

1240 Song, F., Zhang, G., Ramanathan, V. and Ruby Leung, L.: Trends in surface equivalent
1241 potential temperature: A more comprehensive metric for global warming and
1242 weather extremes, *Proc. Natl. Acad. Sci. U.S.A.*, 119, 6,
1243 <https://doi.org/10.1073/pnas.2117832119>, 2022.

1244 Steadman, R. G.: A universal scale of apparent temperature, *J. Appl. Meteorol.*, 23 (12),
1245 1674–1687, [https://doi.org/10.1175/1520-0450\(1984\)023<1674:AUSOAT>2.](https://doi.org/10.1175/1520-0450(1984)023<1674:AUSOAT>2.0.CO;2)
1246 [0.CO;2](https://doi.org/10.1175/1520-0450(1984)023<1674:AUSOAT>2.0.CO;2), 1984.

1247 Steadman, R. G.: Norms of apparent temperature in Australia, *Aust. Meteorol. Mag.*, 43,
1248 1–16, 1994.

1249 Stohl, A., Aamaas, B., Amann, M., Baker, L. H., Bellouin, N., Berntsen, T. K., Boucher,
1250 O., Cherian, R., Collins, W., Daskalakis, N., Dusinska, M., Eckhardt, S., Fuglestvedt,
1251 J. S., Harju, M., Heyes, C., Hodnebrog, Ø., Hao, J., Im, U., Kanakidou, M., Klimont,
1252 Z., Kupiainen, K., Law, K. S., Lund, M. T., Maas, R., MacIntosh, C. R., Myhre, G.,
1253 Myriokefalitakis, S., Olivié, D., Quaas, J., Quennehen, B., Raut, J.-C., Rumbold, S.
1254 T., Samset, B. H., Schulz, M., Seland, Ø., Shine, K. P., Skeie, R. B., Wang, S., Yttri,
1255 K. E., and Zhu, T.: Evaluating the climate and air quality impacts of short-lived
1256 pollutants, *Atmos. Chem. Phys.*, 15, 10529–10566, [https://doi.org/10.5194/acp-15-](https://doi.org/10.5194/acp-15-10529-2015)
1257 [10529-2015](https://doi.org/10.5194/acp-15-10529-2015), 2015.

1258 Su, J., Brauer, M., Ainslie, B., Steyn, D., Larson, T., and Buzzelli, M.: An innovative land
1259 use regression model incorporating meteorology for exposure analysis, *Sci. Total*
1260 *Environ.*, 390, 520-529, <https://doi.org/10.1016/j.scitotenv.2007.10.032>, 2008.

1261 Tong, C., Yim, S., Rothenberg, D., Wang, C., Lin, C., Chen, Y., and Lau, N.: Projecting
1262 the impacts of atmospheric conditions under climate change on air quality over the
1263 Pearl River Delta region, *Atmos. Environ.*, 193, 79-87,
1264 <https://doi.org/10.1016/j.atmosenv.2018.08.053>, 2018.

1265 Torma, C. and Giogi, F.: Assessing the contribution of different factors in regional

1266 climate model projections using the factor separation method, *Atmos. Sci. Lett.*, 15,
1267 239–244, <https://doi.org/10.1002/asl2.491>, 2014.

1268 Upadhyay, A., Dey, S., Goyal, P., and Dash, S.: Projection of near-future anthropogenic
1269 PM_{2.5} over India using statistical approach, *Atmos. Environ.*, 186, 178-188,
1270 <https://doi.org/10.1016/j.atmosenv.2018.05.025>, 2018.

1271 Vandyck, T., Keramidas, K., Saveyn, B., et al.: A global stocktake of the Paris pledges:
1272 Implications for energy systems and economy, *Global Environmental Change*, 41,
1273 46-63, <https://doi.org/10.1016/j.gloenvcha.2016.08.006>, 2016.

1274 Wang, J., Allen, D., Pickering, K., Li, Z., He, H.: Impact of aerosol direct effect on East
1275 Asian air quality during the EAST-AIRE campaign, *J. Geophys. Res.- Atmos.*, 121,
1276 6534-6554, <https://doi.org/10.1002/2016JD025108>, 2016.

1277 Wang, J., Moore, J. C., Zhao, L., Yue, C., and Di, Z.: Regional dynamical and statistical
1278 downscaling temperature, humidity and windspeed for the Beijing region under
1279 stratospheric aerosol injection geoengineering, *Earth Syst. Dynam.*,
1280 <https://doi.org/10.5194/esd-2022-35>, 2022.

1281 Wang, J., Feng, J., Yan, Z., Hu, Y., and Jia, G.: Nested high-resolution modeling of the
1282 impact of urbanization on regional climate in three vast urban agglomerations in
1283 China, *J. Geophys. Res.- Atmos.*, 117(D21), <https://doi.org/10.1029/2012JD018226>,
1284 2017.

1285 Wang, J., Zhang, L., Niu, X., and Liu, Z.: Effects of PM_{2.5} on health and economic loss:
1286 Evidence from Beijing-Tianjin-Hebei region of China, *J. Cleaner Prod.*, 257, 120605,
1287 <https://doi.org/10.1016/j.jclepro.2020.120605>, 2020.

1288 Wang, P., Luo, M., Liao, W., Xu, Y., Wu, S., Tong, X., Tian, H., Xu, F., Han, Y.:
1289 Urbanization contribution to human perceived temperature changes in major urban
1290 agglomerations of China, *Urban Climate*, 38, 100910,
1291 <https://doi.org/10.1016/j.uclim.2021.100910>, 2021.

1292 Wang, S., Ancell, B., Huang, G., Baetz, B.: Improving robustness of hydrologic
1293 ensemble predictions through probabilistic pre- and post-processing in sequential
1294 data assimilation, *Water Resources Research*, 54, 2129–2151,
1295 <https://doi.org/10.1002/2018WR022546>, 2018.

1296 Wang, X., Huang, G., Lin, Q., Nie, X., Cheng, G., Fan, Y., Li, Z., Yao, Y., Suo, M.: A
1297 stepwise cluster analysis approach for downscaled climate projection - a Canadian
1298 case study, *Environ. Model Softw.*, 49, 141–151,
1299 <https://doi.org/10.1016/j.envsoft.2013.08.006>, 2013.

1300 Wang, Y., Hu, J., Zhu, J., Li, J., Qin, M., Liao, H., Chen, K., and Wang, M.: Health
1301 Burden and economic impacts attributed to PM_{2.5} and O₃ in China from 2010 to 2050
1302 under different representative concentration pathway scenarios, *Resour. Conserv.
1303 Recy.*, 173, 105731, <https://doi.org/10.1016/j.resconrec.2021.105731>, 2021.

1304 Wang, Y., Chen, L., Song, Z., Huang, Z., Ge, E., Lin, L., Luo, M.: Human-perceived-
1305 temperature changes over South China: long-term trends and urbanization effects,
1306 *Atmos. Res.*, 215, 116–127, <https://doi.org/10.1016/j.atmosres.2018.09.006>, 2019.

1307 Wang, Y., Yao, L., Wang, L., Liu, Z., Ji, D., Tang, G., Zhang, J., Sun, Y., Hu, N., and Xin,
1308 J.: Mechanism for the formation of the January 2013 heavy haze pollution episode
1309 over central and eastern China, *Sci. China Earth Sci.*, 57, 14-25,

1310 <https://doi.org/10.1007/s11430-013-4773-4>, 2014.

1311 Wang, Y., Zhuang, G., Zhang, X., Huang, K., Xu, C., Tang, A., Chen, J., and An, Z.: The
1312 ion chemistry, seasonal cycle, and sources of PM_{2.5} and TSP aerosol in Shanghai,
1313 *Atmos. Environ.*, 40, 2935-2952, <https://doi.org/10.1016/j.atmosenv.2005.12.051>,
1314 2006.

1315 Watanabe, S., Hajima, T., Sudo, K., Nagashima, T., Takemura, T., Okajima, H., Nozawa,
1316 T., Kawase, H., Abe, M., Yokohata, T., Ise, T., Sato, H., Kato, E., Takata, K., Emori,
1317 S., and Kawamiya, M.: MIROC-ESM 2010: model description and basic results of
1318 CMIP5-20c3m experiments, *Geosci. Model Dev.*, 4, 845–872,
1319 <https://doi.org/10.5194/gmd-4-845-2011>, 2011.

1320 Wei, J., Li, Z., Lyapustin, A., Sun, L., Peng, Y., Xue, W., Su, T., and Cribb, M.:
1321 Reconstructing 1-km-resolution high-quality PM_{2.5} data records from 2000 to 2018
1322 in China: spatiotemporal variations and policy implications, *Remote Sens. Environ.*,
1323 252, 112136, <https://doi.org/10.1016/j.rse.2020.112136>, 2021.

1324 Wilcke, R. A. I., Mendlik, T., Gobiet, A.: Multi-variable error correction of regional
1325 climate models, *Clim. chang.*, 120(4), 871-887, <https://doi.org/10.1007/s10584-013-0845-x>, 2013.

1327 Wu, D., Tie, X., Li, C., Ying, Z., Kai-Hon Lau, A., Huang, J., Deng, X., and Bi, X.: An
1328 extremely low visibility event over the Guangzhou region: a case study, *Atmos.*
1329 *Environ.*, 39, 6568-6577, <https://doi.org/10.1016/j.atmosenv.2005.07.061>, 2005.

1330 Wu, J., Gao, X., Giorgi, F., Chen, D.: Changes of effective temperature and cold/hot days
1331 in late decades over China based on a high resolution gridded observation dataset,
1332 *Int. J. Climatol.*, 37:788–800, <https://doi.org/10.1002/joc.5038>, 2017.

1333 Xu, J., Yao, M., Wu, W., Qiao, X., Zhang, H., Wang, P., Yang, X., Zhao, X., and Zhang,
1334 J.: Estimation of ambient PM_{2.5}-related mortality burden in China by 2030 under
1335 climate and population change scenarios: A modeling study, *Environ. Int.*,
1336 156,106733, <https://doi.org/10.1016/j.envint.2021.106733>, 2021.

1337 Xue, W., Zhang, J., Zhong, C., Li, X., and Wei, J.: Spatiotemporal PM_{2.5} variations and
1338 its response to the industrial structure from 2000 to 2018 in the Beijing-Tianjin-
1339 Hebei region, *J. Cleaner Prod.*, 279, 123742,
1340 <https://doi.org/10.1016/j.jclepro.2020.123742>, 2021.

1341 Yang, S., Ma, Y., Duan, F., He, K., Wang, L., Wei, Z., Zhu, L., Ma, T., Li, H., Ye, S.:
1342 Characteristics and formation of typical winter haze in Handan, one of the most
1343 polluted cities in China, *Sci. Total Environ.*, 613-614, 1367-1375,
1344 <https://doi.org/10.1016/j.scitotenv.2017.08.033>, 2018.

1345 Yang, X., Wu, Q., Zhao, R., Cheng, H., He, H., Ma, Q., Wang, L., and Luo, H.: New
1346 method for evaluating winter air quality: PM_{2.5} assessment using Community
1347 Multiscale Air Quality Modeling (CMAQ) in Xi'an, *Atmos. Environ.*, 211, 18-28,
1348 <https://doi.org/10.1016/j.atmosenv.2019.04.019>, 2019.

1349 Yang, X., Zhao, C., Guo, J., and Wang, Y.: Intensification of aerosol pollution associated
1350 with its feedback with surface solar radiation and winds in Beijing, *J. Geophys. Res.*
1351 *Atmos.*, 121, 4093-4099, <https://doi.org/10.1002/2015JD024645>, 2016.

1352 Yang, Y., Maraun, D., Ossó, A., and Tang, J.: Increased spatial extent and likelihood of
1353 compound long-duration dry and hot events in China, 1961–2014, *Nat. Hazards*

1354 Earth Syst. Sci., 23, 693–709, <https://doi.org/10.5194/nhess-23-693-2023>, 2023.

1355 Yang, Y., and Tang, J.: Substantial Differences in Compound Long - Duration Dry and
 1356 Hot Events Over China Between Transient and Stabilized Warmer Worlds at 1.5° C
 1357 Global Warming, *Earths Future*, 11, e2022EF002994,
 1358 <https://doi.org/10.1029/2022EF002994>, 2023.

1359 Yang, Y., Tang, J., Xiong, Z., Wang, S., and Yuan, J.: An intercomparison of multiple
 1360 statistical downscaling methods for daily precipitation and temperature over China:
 1361 future climate projections, *Clim. Dynam.*, 52, 6749–
 1362 6771, <https://doi.org/10.1007/s00382-018-4543-2>, 2019.

1363 Yin, Z., Wang, H., and Chen, H.: Understanding severe winter haze events in the North
 1364 China Plain in 2014: roles of climate anomalies, *Atmos. Chem. Phys.*, 17, 1641–
 1365 1651, <https://doi.org/10.5194/acp-17-1641-2017>, 2017.

1366 You, T., Wu, R., Huang, G., Fan, G.: Regional meteorological patterns for heavy
 1367 pollution events in Beijing, *J. Meteorolog. Res.*, 31, 597-611,
 1368 <https://doi.org/10.1007/s13351-017-6143-1>, 2017.

1369 Yu, X., Moore, J. C., Cui, X., Rinke, A., Ji, D., Kravitz, B., and Yoon, J.: Impacts,
 1370 effectiveness and regional inequalities of the GeoMIP G1 to G4 solar radiation
 1371 management scenarios, *Global and Planetary Change*, 129, 10-22,
 1372 <https://doi.org/10.1016/j.gloplacha.2015.02.010>, 2015.

1373 Zhan, P., Zhu, W., Zhang, T., Cui, X., Li, N.: Impacts of sulfate geoengineering on rice
 1374 yield in China: Results from a multimodel ensemble, *Earth's Future*, 7(4), 395-410,
 1375 <https://doi.org/10.1029/2018EF001094>, 2019.

1376 Zhang, Q., Zheng, Y., Tong, D., Shao, M., Wang, S., Zhang, Y., Xu, X., Wang, J., He, H.,
 1377 Liu, W., Ding, Y., Lei, Y., Li, J., Wang, Z., Zhang, X., Wang, Y., Cheng, J., Liu, Y.,
 1378 Shi, Q., Yan, L., Geng, G., Hong, C., Li, M., Liu, F., Zheng, B., Cao, J., Ding, A.,
 1379 Gao, J., Fu, Q., Huo, J., Liu, B., Liu, Z., Yang, F., He, K., and Hao, J.: Drivers of
 1380 improved PM_{2.5} air quality in China from 2013 to 2017, *PNAS*, 116, 24463-24469,
 1381 <https://doi.org/10.1073/pnas.1907956116>, 2019.

1382 Zhang, Z., Gong, D., Mao, R., Kim, S., Xu, J., Zhao, X., and Ma, Z.: Cause and
 1383 predictability for the severe haze pollution in downtown Beijing in November–
 1384 December 2015, *Sci. Total Environ.*, 592, 627-638,
 1385 <https://doi.org/10.1016/j.scitotenv.2017.03.009>, 2017.

1386 Zhao, D., Xin, J., Gong, C., Quan, J., Liu, G., Zhao, W., Wang, Y., Liu, Z., and Song, T.:
 1387 The formation mechanism of air pollution episodes in Beijing city: insights into the
 1388 measured feedback between aerosol radiative forcing and the atmospheric boundary
 1389 layer stability, *Sci. Total Environ.*, 692, 371–381,
 1390 <https://doi.org/10.1016/j.scitotenv.2019.07.255>, 2019.

1391 Zheng, C., Zhao, C., Zhu, Y., Wang, Y., Shi, X., Wu, X., Chen, T., Wu, F., and Qiu, Y.:
 1392 Analysis of influential factors for the relationship between PM_{2.5} and AOD in
 1393 Beijing, *Atmos. Chem. Phys.*, 17, 13473–13489, <https://doi.org/10.5194/acp-17-13473-2017>, 2017.

1395 Zhou, B., Xu, Y., Wu, J., Dong, S., and Shi, Y.: Changes in temperature and precipitation
 1396 extreme indices over China: analysis of a high-resolution grid dataset, *Int. J.*
 1397 *Climatol.*, 36, 1051–1066, <https://doi.org/10.1002/joc.4400>, 2016.

1398 Zhu, J., Wang, S., Huang, G.: Assessing Climate Change Impacts on Human-Perceived
1399 Temperature Extremes and Underlying Uncertainties, *Journal of Geophysical*
1400 *Research: Atmosphere*, 124 (7), 3800-3821, <https://doi.org/10.1029/2018JD029444>,
1401 2019.

1402 Zhu, X., Huang, G., Zhou, X., Zheng, S.: Projection of apparent temperature using
1403 statistical downscaling approach in the Pearl River Delta, *Theor. Appl. Climatol.*,
1404 144 (3–4), 1253–1266, <https://doi.org/10.1007/s00704-021-03603-2>, 2021.

1405